HHS Public Access

Author manuscript

Cell Rep. Author manuscript; available in PMC 2023 November 10.

Published in final edited form as:

Cell Rep. 2023 September 26; 42(9): 113070. doi:10.1016/j.celrep.2023.113070.

TMEM127 suppresses tumor development by promoting RET ubiquitination, positioning, and degradation

Qianjin Guo[1], **Zi-Ming Cheng**[1], **Hector Gonzalez-Cantú**[1], **Matthew Rotondi**[1], **Gabriela Huelgas-Morales**[1], **Purushoth Ethiraj**[1], **Zhijun Qiu**[1], **Jonathan Lefkowitz**[1], **Wan Song**[1], **Bethany N. Landry**[1], **Hector Lopez**[1], **Cynthia M. Estrada-Zuniga**[1], **Shivi Goyal**[1], **Mohammad Aasif Khan**[1], **Timothy J. Walker**[2], **Exing Wang**[3], **Faqian Li**[4], **Yanli Ding**[4], **Lois M. Mulligan**[2], **Ricardo C.T. Aguiar**[1,5,6], **Patricia L.M. Dahia**[1,5,7,*]

[1]Division of Hematology/Medical Oncology, Department of Medicine, University of Texas Health San Science Center at Antonio (UTHSCSA), San Antonio, TX, USA

[2]Division of Cancer Biology and Genetics, Cancer Research Institute, Queen's University, Kingston, ON, Canada

[3]Department Cell Structure and Anatomy, UTHSCSA, San Antonio, TX, USA

[4]Department of Pathology, UTHSCSA, San Antonio, TX, USA

[5]Mays Cancer Center, UTHSCSA, San Antonio, TX, USA

[6]South Texas Veterans Health Care System, Audie Murphy VA Hospital, San Antonio, TX 78229, USA

[7]Lead contact

SUMMARY

The *TMEM127* gene encodes a transmembrane protein of poorly known function that is mutated in pheochromocytomas, neural crest-derived tumors of adrenomedullary cells. Here, we report that, at single-nucleus resolution, *TMEM127*-mutant tumors share precursor cells and transcription regulatory elements with pheochromocytomas carrying mutations of the tyrosine kinase receptor *RET*. Additionally, *TMEM127*-mutant pheochromocytomas, human cells, and mouse knockout models of TMEM127 accumulate RET and increase its signaling. TMEM127 contributes to RET cellular positioning, trafficking, and lysosome-mediated degradation. Mechanistically, TMEM127 binds to RET and recruits the NEDD4 E3 ubiquitin ligase for RET ubiquitination and degradation via TMEM127 C-terminal PxxY motifs. Lastly, increased cell

*Correspondence: dahia@uthscsa.edu.

AUTHOR CONTRIBUTIONS

Conceptualization, Q.G., P.L.M.D., and R.C.T.A.; snRNA-seq and bioinformatics, Q.G.; molecular studies, Q.G., Z.-M.C., M.R., H.G.C, M.A.K., W.S., B.N.L., C.E.Z., H.K., M.A.K., S.G., P.E., and Z.Q.; mouse models, Q.G., P.E., and Z.Q.; confocal microscopy, Q.G., G.H.-M., W.S., and E.W.; pathology, Y.D. and F.L.; resources, Q.G., H.C.G., H.L., S.G., R.C.T.A., T.J.W., L.M.M., and P.L.M.D.; writing, Q.G., R.C.T.A., and P.L.M.; supervision, P.L.M.D.; funding acquisition, R.C.T.A. and P.L.M.D.

SUPPLEMENTAL INFORMATION

Supplemental information can be found online at https://doi.org/10.1016/j.celrep.2023.113070.

DECLARATION OF INTERESTS

The authors declare no competing interests.

proliferation and tumor burden after TMEM127 loss can be reversed by selective RET inhibitors *in vitro* and *in vivo*. Our results define TMEM127 as a component of the ubiquitin system and identify aberrant RET stabilization as a likely mechanism through which *TMEM127* loss-of-function mutations cause pheochromocytoma.

Graphical Abstract

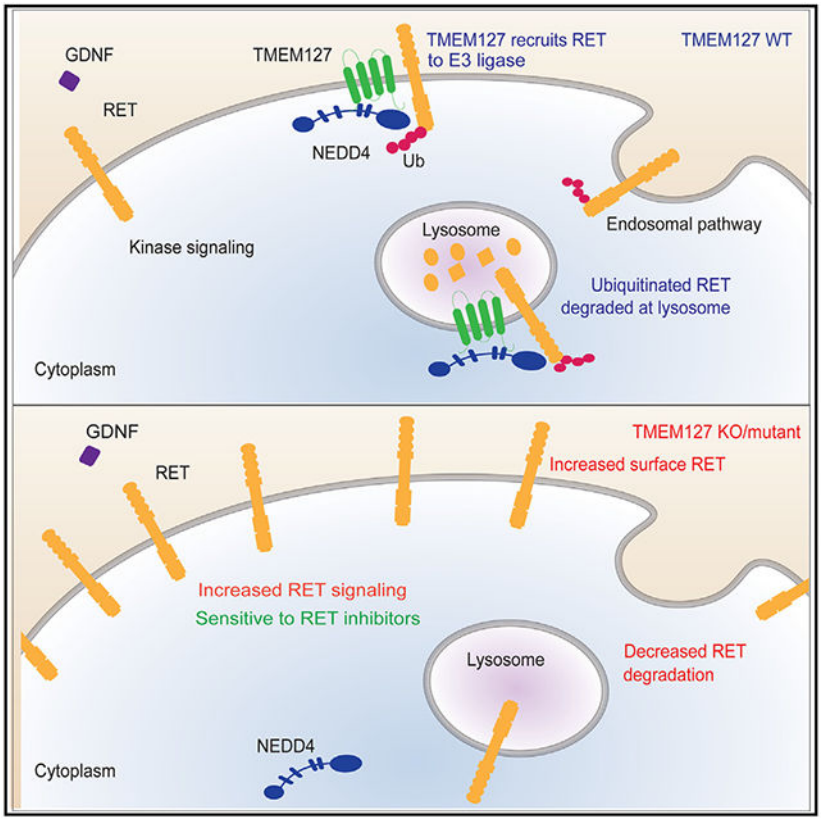

In brief

Guo et al. report that TMEM127 deficiency leads to pheochromocytoma by reducing NEDD4-mediated RET ubiquitination, positioning, and degradation and that the resulting cell proliferation is responsive to RET selective inhibition.

INTRODUCTION

Pheochromocytomas and paragangliomas (PPGLs) are rare tumors derived from the neural crest that arise from chromaffin cells of the adrenal gland or extra-adrenal paraganglia, respectively.[1] These tumors are known for their high heritability rates and for carrying single driver events that are mutually exclusive.[1] *TMEM127* is a tumor suppressor gene that we identified as a susceptibility gene to PPGLs through loss-of-function germline mutations.[2] This gene is conserved in vertebrates and encodes a ubiquitously expressed transmembrane protein[2]; however, the mechanism of TMEM127 tumor suppression remains poorly defined.

Molecular classification of PPGLs has defined discrete clusters that are driven by the causative mutation.[3] PPGLs carrying germline *TMEM127* mutations belong to the kinase cluster (also known as "cluster 2").[2,4] A prototypical member of the PPGL kinase cluster includes tumors with *RET* mutations, suggesting that these two genes might regulate congruent signals.[1]

We previously showed that TMEM127 loss leads to the activation of mammalian target of rapamycin (mTOR), a converging hub of various kinase signals, including those related to RET activation, strengthening potential links between TMEM127- and RET-related pathways.[2] We also found that TMEM127 undergoes endocytosis[5] and is associated with the plasma membrane, early endosomes, and lysosomes in response to nutrient challenges.[6,7] In contrast, tumor-derived mutations often lead to expression of a diffuse, unstable cytosolic TMEM127 or mutants that are retained on the plasma membrane,[5] supporting its potential role in trafficking through the endomembrane system. Interestingly, TMEM127 was identified to facilitate bacterial infection by promoting the degradation of major histocompatibility complex class II (MHC-II)[8] through ubiquitin-mediated pathways, suggesting a potential mechanism by which TMEM127 can relay extracellular signals.

The *RET* gene encodes a tyrosine kinase receptor that is expressed in neural crest-derived tissues and the developing kidney.[9] This receptor is activated by a ligand/coreceptor complex, glial cell line-derived neurotrophic factor (GDNF)/GFRα1, which leads to RET dimerization, followed by autophosphorylation and activation of signaling through RAS/mitogen-activated protein kinase (MAPK), phosphatidylinositol 3-kinase (PI3K)/AKT, STAT, and PLC-γ pathways.[10,11] RET has a broad role in cancer: through germline gain-of-function mutations, it causes multiple endocrine neoplasia type 2A (MEN 2A) or type 2B (MEN 2B), associated PPGLs, and medullary thyroid carcinoma (MTC).[9] Somatically, *RET* is mutated in PPGLs and MTCs or can be disrupted by gene fusions in lung and thyroid, and also in pheochromocytomas.[12,13] Additionally, overexpression of the wild-type (WT)-RET in breast and pancreatic cancers can result in its abnormal activation.[9]

Here, we show that TMEM127 deficiency leads to aberrant RET accumulation, activation, and surface expression associated with attenuated NEDD4-mediated RET ubiquitination and degradation. These findings define TMEM127 as a RET antagonist, explaining the similarities between pheochromocytomas driven by *RET* and *TMEM127* mutations.

RESULTS

TMEM127-mutant tumors are closely related to *RET*-mutant tumors by molecular profiling

We reported earlier that PPGLs carrying either *RET* or *TMEM127* mutation display overlapping features.[2,4] Clinically, tumors from these two genotypes are preferentially located in the adrenal (pheochromocytomas), as opposed to extra-adrenal paraganglia (i.e., paragangliomas), predominantly secrete epinephrine, the terminal catecholamine produced by chromaffin cells, can occur bilaterally, and rarely progress to metastases.[14-16] Transcriptionally, they share a profile related to kinase signaling.[2-4,17] Thus, we hypothesized that these two genotypes potentially share mechanisms of tumorigenesis. Using gene expression profile on microarrays, we found that *TMEM127*-mutant

pheochromocytomas show similar *RET* mRNA expression to tumors with *RET* mutations, in contrast with tumors belonging to the other main group, cluster 1 (Figure S1A, left). Additionally, this result was independently validated in both our RNA sequencing (RNA-seq) cohort and a publicly available (The Cancer Genome Atlas [TCGA])[3] dataset (Figure S1A, right; Table S1). These cohorts lacked normal adrenal medulla; however, based on normal adrenals from a publicly available dataset,[18] RET transcript is decreased in chromaffin cells of cluster 1 tumors, while expression in cluster 2 tumors is more variable and can be similar to normal adrenal medulla (Figure S1B), as previously suggested.[18-21]

TMEM127- and *RET*-mutant tumors share developmental trajectory and regulatory activation drivers at the single-nucleus level

To gain further insight into *TMEM127*- and *RET*-related tumors at single-cell resolution, we generated single-nucleus RNA-seq (snRNA-seq) data from pheochromocytomas carrying these mutations (n = 3 and n = 2, respectively) employing an optimized workflow (Figure 1A) and analyzed 35,752 nuclei (Table S2; Figure S1C). Bioinformatics was performed as detailed in STAR Methods.[22,23] We first used a uniform manifold approximation and projection (UMAP) plot[24,25] to visualize the transcriptomes and identified 11 clusters (Figures 1B and 1C; Table S3), spanning the range of cell types expected for adrenal glands[23,26,27] and PPGLs.[18] Expectedly, we found the most abundant cluster to contain chromaffin cells (Figures 1B and 1C).

We verified the identity of the clusters containing tumor cells using the InferCNV algorithm to estimate copy number variations (CNVs). This approach revealed chromosome 1p (Chr1p) deletion in the chromaffin-related clusters of four of the five tumors (Figures 1D, 1E, and S1D-1G). Chr1p loss is a well-established structural CNV shared by ~80% of pheochromocytomas belonging to the kinase group.[3,4,28] Reassuringly, the typical *TMEM127* signature of Chr2q loss, encompassing the TMEM127 locus,[2,29] was detected in the *TMEM127* mutant tumors and was absent from *RET* tumors (Figures 1D, 1E, and S1D-1G). Schwann cell precursors had been proposed as the originators of 80% of chromaffin cells during mouse adrenal development[30]; however, in our tumor samples, Schwann cell marker-positive (SCP) nuclei (Figures 1D and 1E) did not share the CNVs found in the chromaffin clusters (Figures S1E-S1H). These results agree with recent reports of postnatal human pheochromocytomas[18] or lineage-related neuroblastomas tumors[26] and suggest that SCPs may represent differentiated Schwann cells.

In our samples, the neoplastic clusters recognized by the expression of a panel of classic noradrenergic and adrenergic markers, including *TH* and *CHGA*, had noticeable substructure, suggesting heterogeneity of these cells (Figure 1F). Based on expanded analysis involving other markers of precursor chromaffin cells (for example, *CARTPT, CHRNA3, CHRNA7, EIF4A3*),[18,26] progenitor cells (*RTTN, SOX10, ERBB3*),[26] neuroblasts (*PTPRD, UNC5D*), cell cycle genes (*BUB1, MKI67, TOP2A*), and others, four chromaffin cell (CC) subclusters, CC1 through CC4, were identified (Figures 1C, and 1G; Table S3). We found no genotype-exclusive cluster (Figure S1H); however, the proportions of cells (nuclei) varied between the *RET* and *TMEM127*-related tumor clusters: the *TMEM127* tumors were more abundantly distributed in CC2 and the *RET* tumor nuclei

were enriched in CC3, while both genotypes were more similarly represented in CC1 and in the cell cycle marker-enriched CC4 cluster (Figures S1H and S1I). To gain insight into the attributes of these four chromaffin clusters, we applied several methods to infer their dynamic ordering. Using SLICE,[31] cluster CC4 showed the highest instability and greater potential to differentiate (Figure 1H), supporting a role for this cluster as the "earliest" subpopulation along a hierarchical differentiation trajectory, while the SCP cluster showed the highest stability, consistent with a differentiated, nonneoplastic cell type (Figure 1H). Monocle[32] estimated a pseudotime trajectory with CC4 also as the earliest chromaffin tumor cell subpopulation followed by CC1, and then branching into CC2 (enriched in TMEM127-derived tumor cells) or into CC3 (enriched with cells from RET-derived tumors; Figure S1J). Cytotrace[33] displayed a similar ordering inference, shown by each represented genotype (Figure 1I). These results support a similar developmental trajectory for *TMEM127*- and *RET*-mutant pheochromocytomas, as previously presumed by clinical observations[34,35] and by recent observations.[18] We next explored the genes characteristic of the *TMEM127* mutation profile by comparing the signature of CC2 and CC3. We found 127 gene sets differentially expressed between clusters CC2 and CC3 at false discovery rate (FDR) <25% (Table S4), with enrichment for plasma membrane and cell-cell signaling pathways in the *TMEM127* group (Figures S1K; Table S5).

Single-nucleus signature of *TMEM127* deficiency is conserved in mice and humans

To expand these observations to a separate *in vivo* model of *TMEM127*-associated signature, we generated snRNA-seq data from adrenals of mice lacking *Tmem127*. These mice are viable and do not develop spontaneous pheochromocytomas/paragangliomas,[36] offering insight into the "preneoplastic" state of the *Tmem127*-deficient CCs. Using the same protocol of PPGLs (Figure 1A), we processed frozen adrenals from three knockout (KO) and three WT adult mice and analyzed 21,274 nuclei (Table S6), from which we recognized 19 distinct clusters (Figures 2A and 2B; Table S7). CCs were distributed into two clusters, one with low expression of *Pnmt*, the gene encoding phenylethanolamine N-methyltransferase, the enzyme that converts norepinephrine into epinephrine and that we referred to as the "immature" chromaffin cluster (ICC–, $Pnmt^{-}$), and another representing the more "mature" chromaffin markers (mature CCs [MCCs] or $Pnmt^{+}$) Figures 2A-2C). Like the pheochromocytoma snRNA-seq dataset, we did not find a genotype-exclusive cell cluster (Figure S2A) but noticed differential proportions between WT and KO samples (Figure S2B), with enrichment of MCC/$Pnmt^{+}$ and stromal cell KO, compared to WT, nuclei (Figure S2D). This pattern aligns with the biochemical profile of *TMEM127*-mutant human pheochromocytomas, which express PNMT and are predominantly epinephrine-producing tumors.[16] Analysis of cell cycle genes showed higher G2/M representation in MCC/$Pnmt^{+}$, but not ICC($Pnmt^{-}$), of KO nuclei, suggesting an enhanced proliferative potential (Figure 2D; Chi-squared test, $p = 0.012$). We confirmed an enrichment for genes involved in proliferative pathways in the KO MCCs (Figures 2E; Table S8), suggesting that these cells are primed for growth, while stromal (Figure S2C) or SCP (Figure S2D) cells did not show proliferative preference in KO cells. We next used SCENIC[37] to identify potential regulatory networks that might characterize MCCs. The MCC regulon showed activation of various transcription factors, including those related to the immediate-early gene (IEG) response (e.g., *Egr1*) and, as expected, those associated with the neural crest, such as

Phox2b (Figure 2F). The *Egr1* regulatory profile was uniquely enriched in KO MCCs (Figures S2E and S2F). We validated the *Egr1* expression and location in the mouse adrenal medulla by confocal microscopy (Figure S2G). To relate this finding with human tumors, we examined the *EGR1* expression in pheochromocytoma snRNA-seq. We found that *EGR1* was highly expressed in the tumor clusters, especially the developmentally "precursor" clusters (CC4 and CC1; Figure 2G). We extended this observation to a publicly available snRNA-seq cohort and found that pheochromocytomas belonging to the kinase/cluster 2 group, including *TMEM127* and *RET* mutants, show a trend toward higher *EGR1* transcript compared to those in cluster 1 (Figure S2H). Concordant results were seen in a separate cohort of primary tumors showing higher EGR1 protein levels in cluster 2 (Figure 2H) and agree with previous observations supporting the role of EGR1 in *RET*-related tumorigenesis.[38-40] Likewise, the "MCC signature" of the KO mice (Table S8) was also enriched in the CC4 and CC1 clusters of the human PPGL (Figure 2I) using AUCell.[41]

These results suggest conserved mechanisms between the signatures of *Tmem127*-KO mouse adrenals and human pheochromocytomas. Moreover, these analyses reveal shared early developmental tumor populations (CC4, CC1) and transcriptional regulators such as EGR1 in tumors carrying *RET* or *TMEM127* mutations. Overall, our data indicate strong similarity between tumor cells with *RET* or *TMEM127* mutations at the single-cell transcription level and, together with the enriched signatures of plasma membrane and cell-cell signaling in *TMEM127* mutant pheochromocytomas, suggest that mechanistic distinctions between these two genotypes may occur predominantly at a post-transcriptional level.

TMEM127 mutations or loss result in RET protein accumulation and signaling activation

To explore post-transcriptional features of *TMEM127*- and *RET*-related tumors, we examined protein extracts and found that samples from cluster 2 had higher RET protein levels than those from cluster 1 tumors (Figures 3A and S3A). These findings were confirmed by RET immunohistochemistry (IHC) of archival PPGLs (Figure 3B). In our cohort, *TMEM127*-mutant tumors had generally higher RET levels than other cluster 2 samples (Figures 3A and S3A).

To evaluate this observation, and in the absence of a well-established human pheochromocytoma cell line, we used CRISPR-Cas9 to create TMEM127 KO SH-SY5Y neuroblastoma cells, which are also adrenomedullary in origin and have been widely employed in studies of RET signaling.[42-45] We generated polyclonal TMEM127-KO SH-SY5Y cells with guide RNAs targeting *TMEM127*'s exons 2 (T2-KO) or exon 4 (T4-KO) that we validated previously in other cell lines.[5,6,36] We found that both T2-KO and T4-KO cells had elevated RET levels (Figure 3C), replicating the findings of *TMEM127*-mutant pheochromocytomas.

Furthermore, adrenals from whole-body *Tmem127*-KO mice also showed higher Ret protein expression than WT counterparts (Figure 3D). In these adrenals, Ret expression remained restricted to the adrenomedullary cells (Figure S3B), as in previous reports.[46,47] In contrast, *Ret* transcript levels were not significantly different between *Tmem127*-KO and control adrenals (Figure S3C), nor between KO and WT SH-SY5Y cells (Figure S3D).

Reconstitution of KO SH-SY5Y cells with TMEM127-WT was sufficient to reverse RET accumulation, while expression of TMEM127-G37R, a patient-derived loss-of-function mutant,[5] did not have the same effect (Figure 3E), in support of a requirement for functional TMEM127 for this effect. RET accumulation was associated with high RET autophosphorylation in *TMEM127*-mutant primary tumors (Figure 3A). Likewise, phosphorylation of RET and its downstream signaling effectors AKT and ERK/MAPK was also increased in TMEM127-KO cells exposed to the RET ligand GDNF (Figure 3F). These results suggested that RET signals are hyperactive after TMEM127 loss, possibly due to the higher abundance of RET in these cells.

Together, three independent models of TMEM127 deficiency (i.e., human pheochromocytomas, human cell lines, and mouse adrenals) support increased RET protein accumulation as a conserved feature associated with TMEM127 loss.

TMEM127 affects RET turnover and degradation

To gain insights into the mechanisms through which WT TMEM127 might downregulate RET, we evaluated RET clearance after protein synthesis inhibition with cycloheximide (CHX). RET protein was undetectable 8 h after CHX exposure in TMEM127-WT cells but was clearly visible in cells lacking TMEM127 (Figure 4A), suggesting that TMEM127 acts at the level of RET degradation.

Additionally, while two RET bands of 175 and 155 kDa were detectable in control SH-SY5Y cells, TMEM127-KO cells showed higher levels of both, with predominance of the larger RET band (Figures 4A, 3C, and 3E). The 175-kDa band corresponds to mature, fully glycosylated RET, which is preferentially expressed at the cell surface, and the 155-kDa band represents immature, partially glycosylated RET located predominantly at the endoplasmic reticulum (ER) and Golgi.[48,49] Primary tumors with *TMEM127* mutant, like RET mutants, also expressed predominantly the larger RET band (Figure 3A, longer exposure), suggesting that this was not a cell culture artifact. The higher abundance of 175-kDa RET might imply that TMEM127 functions at the maturation step of RET processing or RET localization. To examine these alternatives, we evaluated the ER to Golgi transition, the site of initial RET maturation,[49] by exposing these cells to an inhibitor of this step, brefeldin A. Brefeldin A treatment led to induction of BiP, a resident ER protein that is activated by ER stress and ER-Golgi transport modifiers.[50] Expectedly, control cells showed a shift toward the immature RET band after brefeldin A, while KO cells had virtually no change (Figure 4B), suggesting that the RET accumulation occurred at a post-Golgi level. We also established that the 175-kDa RET of KO cells corresponded to the fully glycosylated mature RET (Figure S4A) and not to a distinct, aberrant posttranslational modification by exposing cell lysates to peptide-N-glycosidase F (PnGase F),[49,51] which hydrolyzed N-glycosylation sites and recovered unglycosylated RET (120 kDa) in both control and TMEM127-KO cells.

RET glycosylation at the Golgi is pH sensitive,[49] and we previously reported that vATPase-dependent acidification is required for TMEM127 association with lysosomal proteins.[6] Therefore, we used the vATPase inhibitor bafilomycin to test if the RET accumulation in TMEM127-KO cells was dependent on pH-sensitive membrane vesicles such as the lysosome and Golgi.[49,52] Bafilomycin led to RET increase in control cells but had

minimal impact in TMEM127-KO cells (Figure S4B). Similar results were obtained with the lysosome inhibitors chloroquine (Figure 4C) and leupeptin (Figure S4C). Addition of chloroquine to TMEM127-KO cells reconstituted with TMEM127 partially recovered RET accumulation (Figure 4C). Conversely, the proteasome inhibitor bortezomib did not lead to RET accumulation in control or KO cells (Figure S4D). These findings, together with the brefeldin experiments (Figure 4B), support a post-Golgi impact of TMEM127 toward RET and suggest that TMEM127 modifies RET lysosomal degradation.

TMEM127 affects RET distribution to the cell surface

As both TMEM127[2,5-7] and RET[9] undergo endocytosis and are detected at various endomembrane vesicles, we evaluated whether loss of TMEM127 might affect RET membrane association and detected no RET in soluble cell fractions of TMEM127-KO SH-SY5Y cells (Figure S4E). We next investigated if TMEM127 deficiency affected RET distribution within membrane domains using confocal microscopy. In SH-SY5Y-KO cells, endogenous RET showed higher colocalization with the cell surface marker CD56 than control cells (Figure 4D). This was confirmed by expression of a RET-mCherry construct, which showed significantly higher levels of cell surface association in TMEM127-deficient compared to control SH-SY5Y cells, as measured by colocalization with a different surface marker, wheat germ agglutinin (WGA) (Figure S4E).

These results were replicated in an independent cell line, HeLa, modified with the same TMEM127-KO guide RNA. HeLa cells have a larger cytoplasmic area, amenable to distinctive imaging and quantification of signals. Moreover, these cells showed the expected pattern of colocalization of RET and TMEM127 with early endosome and lysosomal vesicles[2,5-7,48,53] (Figure S4G) and measurable modulation of RET levels by TMEM127 genotype modification, similar to SH-SY5Y cells (Figure S4H). In HeLaTMEM127-KO cells, RET-mCherry expression was also shifted to the surface, and this distribution was rescued by re-expression of WT-TMEM127, but not by a membrane-associated TMEM127 mutant derived from a patient with pheochromocytoma[5] (Figure 4E). Additionally, cells lacking TMEM127 had significantly lower levels of endosomal and lysosomal RET compared to control cells, as measured by decreased association of RET with EEA1 (Figure 4F) and with LAMP1 (Figure 4G). These findings, in combination with our results above, are consistent with an effect of TMEM127 in modifying RET subcellular distribution and movement through the endosome and lysosome.

TMEM127 and RET interact in a complex

To examine the generality of these findings, we also evaluated the expression of RET in HEK293FT cells genetically modified using the same TMEM127 guide RNA approach[5] and tested whether TMEM127 re-expression was capable of downregulating functionally altered RET, using the variant forms listed in Figure 5A, which we validated by GDNF and GFRα1 exposure and measurement of phosphorylated ERK (p-ERK) (Figure S5A). We found that an oncogenic RET mutant that is constitutively active and capable of self-dimerizing, RET C634R, the most commonly mutated residue in pheochromocytomas,[10] was as efficiently suppressed by TMEM127 as WT-RET (Figure 5B). Likewise, TMEM127 expression was capable of reducing the levels of a catalytically dead RET mutant, K758M (Figure 5B),

and of a truncated construct encoding the first 1,013 amino acids of RET, which retained its catalytic domain but lacked key residues carrying the RET degron site and the docking site for adaptor proteins and downstream activation (Figure 5B).[9,45,54] These experiments suggest that TMEM127 targets RET independently of its kinase activity or critical C-tail signaling domains.

These results with truncated RET might also suggest that TMEM127 affects the two main alternatively spliced isoforms, RET9 and RET51,[9] as these forms differ only at the C-terminal amino acids, downstream of residue 1,013 (Figure 5A). Our experiments above were performed with a construct expressing RET51, so we next evaluated whether TMEM127 affected RET9. These two isoforms share many signaling properties but also have unique trafficking, turnover, response to ligand exposure, and distinct biological contexts: RET9 is relevant during development and RET51 is the main isoform expressed in oncogenic RET mutations.[9,40,44,45,48,53] We found that both RET9 and RET51 isoforms were modulated by TMEM127 (Figure 5C), consistent with the findings of RET 1–1,013 construct (Figure 5A).

We also examined these two isoforms in SH-SY5Y cells. In the absence of isoform-specific RET antibodies to evaluate endogenous levels of RET9 and RET51 proteins, we transduced the same constructs used in HEK293FT cells and detected each isoform with a tag antibody (myc). We found that, while both RET51 and RET9 accumulated in KO cells (Figure S5B), the increase in RET51 levels was more marked than that of RET9, and this was independent of the efficiency of delivery of these two ectopic constructs to cells (Figure S5C), or changes in isoform-specific RET transcript (Figure S3D). As RET51 is the most abundant isoform expressed at the cell surface,[48,53] this may account for the difference in accumulation between these two isoforms in TMEM127 deficiency. Our results suggest that TMEM127 downregulates both RET isoforms at the post-transcriptional level and these findings are conserved across different cell lineages.

Based on the broad effect of TMEM127 toward several RET forms, we considered whether TMEM127 and RET might interact. Using coimmunoprecipitation experiments in HEK293FT cells expressing both TMEM127 and RET, we found that FLAG-TMEM127 was detected in RET-myc pull-down lysates, along with GRB2, a known RET binding partner (Figure S5D). Reciprocally, GFP-TMEM127 immunoprecipitation (IP) (Figure S5E) recovered RET-myc. Of greater physiological relevance, IP of endogenous RET in SH-SY5Y cells recovered endogenous TMEM127 (Figure 5D). Additionally, we found that catalytically inactive RET (K758M)and RET 1–1,013 co-immunoprecipitated TMEM127 (Figures 5E and S5E), suggesting that the interaction between TMEM127 and RET does not require its kinase activation or C-terminal domains.

TMEM127 PxxY motifs are functionally relevant

Our earlier experiments identified functionally relevant domains for endocytosis and subcellular localization spanning amino acids 203–211 of the TMEM127 C terminus (Figure 5F).[5] Closer inspection of downstream amino acids revealed two putative PxxY (also known as PPxY or PY) motifs (Figure 5F) involving amino acids 233–236, encoding the canonical PPAY, and a potential second motif spanning residues 221–224 (PAEY). PY motifs are

recognition binding sites for WW domain-containing proteins, including prominently the HECT family of E3 ubiquitin ligases.[55-57] Recently, TMEM127 was identified in a screen of modifiers of *Salmonella* infection and its C-terminal domain contributed to TMEM127 association with the HECT-E3 ligase WWP2 to facilitate ubiquitin-mediated degradation of MHC-II, thus enabling cellular entry of the pathogen.[8] We thus assessed the ability of the two putative C-terminal PY motifs of TMEM127 to reduce RET levels. Consistent with the functional relevance of these motifs, expression of TMEM127-Y236A,[8] TMEM127-Y224A, and double (Y224A/Y236A) mutants in TMEM127-KO cells, while still capable of reducing RET levels relative to an empty vector control, were significantly less efficient in reversing RET accumulation compared to the expression of WT-TMEM127 (Figures 5G and S6A). We confirmed the impact of the Y236A mutation on RET levels in SH-SY5Y-KO cells at baseline or after GDNF stimulation (Figure S6B). Additionally, we found that the TMEM127-Y236A mutant retained a punctate profile but had significantly higher expression at the cell surface than WT-TMEM127, and nearly as much as an endocytic-deficient TMEM127 mutant, M214fs, a plasma membrane-bound variant derived from a patient with germline TMEM127 mutation[5] (Figure S6C), suggesting that the Y236A mutation impairs TMEM127 internalization. Notably, the Y236A mutant was deficient in reversing the RET cell surface profile observed in TMEM127-KO cells (Figure 5H), in further support of its functional relevance. Interestingly, neither Y236A nor the double PY mutant (Y224A/Y236A) prevented interaction between TMEM127 and RET (Figures 5I and S6D), suggesting that these residues are not the main interacting site for RET-TMEM127 association. Together, these results point to the relevance of the TMEM127 PY motifs for regulation of RET abundance but not to its association with the receptor.

TMEM127 recruits NEDD4 and targets RET for ubiquitination

In view of these findings, we hypothesized that TMEM127 might affect RET abundance through ubiquitination. To investigate this hypothesis, we performed ubiquitin IP in WT TMEM127 or KO HEK293FT cells ectopically expressing RET and the GFRα1 coreceptor, a model that recapitulates GDNF-mediated RET activation followed by its ubiquitination.[45] In these experiments, RET ubiquitination levels were lower in TMEM127-KO cells than in WT (Figure 6A). Reconstitution of KO cells with WT TMEM127 increased RET ubiquitination, while this effect was blunted in KO cells expressing the TMEM127-Y236A mutant (Figure 6A). These findings suggested that TMEM127 alters RET ubiquitination.

We reasoned that NEDD4, the founder member of the HECT-E3 ligase family, active in neural tissue,[56,57] was a candidate to mediate this modification, since it had been previously reported to interact with, and ubiquitinate, RET9.[45] We confirmed this earlier finding by recovering RET9 from NEDD4 IP in cells that expressed TMEM127 (Figure S7A) and discovered that RET51 also interacted with NEDD4 (Figure 6B). Furthermore, concordant with a potential role of NEDD4 on regulation of RET abundance, in cells rescued with TMEM127, co-expression of NEDD4-WT further downregulated RET levels, while co-expression of a dominant negative, catalytically inactive version of NEDD4 carrying a C867A mutation on the HECT domain, NEDD4-DD,[58] did not (Figure 6C). Conversely, expression of either NEDD4-WT or NEDD4-DD had no significant impact on RET levels in cells lacking TMEM127 (Figure 6D). Next, we found that, in TMEM127-WT cells,

expression of NEDD4, but not NEDD4-DD, increased RET51 ubiquitination levels, in support of RET51 acting as a NEDD4 substrate (Figure 6E). In contrast, in cells lacking TMEM127, expression of NEDD4-WT did not enhance RET ubiquitination and mimicked the effect of NEDD4-DD (Figure 6F). These results suggest that TMEM127 is required for NEDD4 to alter RET ubiquitination and abundance. Notably, although NEDD4 expression failed to increase RET ubiquitination in TMEM127-KO cells, induction of ubiquitination by GDNF was still observed in these cells (Figure 6F), suggesting that the effect of TMEM127 toward RET ubiquitination may be selective and implying that other E3 ligase(s) remain active. This is further suggested by the observation that NEDD4-DD did not completely recapitulate the effect of TMEM127 loss on RET abundance (Figure 6C) or ubiquitination (Figure 6F). However, we found no binding between TMEM127 and CBL (Figure S7B), which has been recognized to have ubiquitin activity toward RET.[45,54]

We determined that NEDD4 was capable of co-immunoprecipitating TMEM127 regardless of the presence of RET (Figure 6G). In contrast, mutation of one (Y236) or both (Y224/Y236) PY motifs at the C terminus of TMEM127 disrupted its interaction with NEDD4, either in the presence (Figure 6H) or absence of RET (Figure S7C). Similar results were obtained with the reciprocal pull-down of GFP-TMEM127 and its mutant forms (Figure S7D), suggesting that the PY motifs are likely the binding sites between TMEM127 and NEDD4. In contrast, neither RET9 (Figure S7E) nor RET51 (Figure S7F) was capable of immunoprecipitating NEDD4 or its catalytically dead version in the absence of TMEM127, suggesting that TMEM127, through its PY sites, bridges the RET-NEDD4 interaction. Furthermore, the defective ability of TMEM127 Y236A to reverse the RET surface distribution of TMEM127-KO cells shown above (Figure 5H) supports NEDD4 as an effector of the actions of TMEM127 on RET subcellular positioning.

NEDD4 predominantly catalyzes K63-linkage polyubiquitination,[59] and these modifications have been associated with endosomal trafficking and lysosomal degradation.[60] To gain insight into the type of ubiquitin linkages associated with RET in these cells, we evaluated K63 and K48 polyubiquitination in these samples. We found that K63-linkage polyubiquitination followed a similar profile to that of TMEM127-KO before and after TMEM127 reconstitution, while K48 did not show TMEM127-dependent variation (Figure 6I). Consistent with a K63-mediated ubiquitination and its role on lysosomal degradation, TMEM127-KO cells had low lysosomal RET levels (Figure 6J), and this profile could not be rescued by cells expressing TMEM127-Y236A, which are incapable of NEDD4 association and are thus ubiquitination defective (Figure 6J). These results suggest that TMEM127 coordinates NEDD4-mediated RET ubiquitination and lysosomal degradation.

Oncogenic effects of TMEM127 loss are RET dependent

To determine whether the tumorigenic phenotype derived from TMEM127 deficiency was related to excessive RET accumulation, we examined cell proliferation in SH-SY5Y cells and found that TMEM127-KO cells had higher proliferation rate (Figure 7A) and viability (Figure 7B) than control cells. Notably, treatment of TMEM127-KO cells with the clinical grade RET inhibitor selpercatinib[61] led to significant growth suppression (Figures 7A and S8A) and RET signaling inhibition (Figure S8B). To provide further confirmation of RET

dependence, we knocked out TMEM127 in SH-SY5Y RET-KO cells[62] using the same guides as in our original SH-SY5Y cells (KO-2 and KO-4; Figure 7B). The viability of these cells was not modified by TMEM127-KO or selpercatinib treatment (Figure 7C), supporting RET as a critical TMEM127 target in this model.

Last, we performed *in vivo* experiments by generating SH-SY5Y-WT or TMEM127-KO xenografts in nude mice. Mice engrafted with TMEM127-KO SH-SY5Y cells developed larger tumors (Figure 7D) and, upon sacrificing, displayed larger tumor burden (Figure 7E) than those injected with TMEM127-WT control cells. Treatment with selpercatinib for 8 days caused significant regression of TMEM127-KO-derived tumors (Figures 7D, 7E, and S8C). These results suggest that TMEM127 deficiency leads to RET-dependent tumorigenesis.

DISCUSSION

In this study, we show that *TMEM127* acts as a tumor suppressor by antagonizing the RET kinase receptor signals. Our data indicate that TMEM127 loss phenocopies RET activation in CCs, providing a compelling mechanism for the clinical similarities and tight molecular association between pheochromocytomas with mutually exclusive mutations in these genes.[2-4,28,63] Our data suggest that TMEM127 antagonism of RET is a route through which TMEM127 suppresses pheochromocytoma development (Figure 7F).

Transcription similarities between PPGLs with mutually exclusive *RET* and *TMEM127* mutations were recognized earlier.[2,4] Our results show that these similarities are evolutionarily conserved in mice and are reproduced at the single-cell resolution. The tumor cells from these two genotypes share similar transcription trajectory and common regulatory drivers, while preserving individual genomic properties such as chromosomal disruptions, as recently corroborated in pheochromocytomas and paragangliomas of various genotypes.[18] Our findings point to posttranslational events as dominant drivers of the distinction between *TMEM127*- and *RET*-related tumorigenesis.

We discovered that TMEM127 controls RET degradation, predominantly of its mature form, which is preferentially located on the cell surface and is primed for activation. In our model, TMEM127 also remains capable of suppressing catalytically inactive RET, or RET lacking its degron sequence at the C terminus. This is distinct from other regulatory mechanisms that couple ligand-mediated RET engagement and activation to a termination signal through ubiquitination.[45,54] It remains to be determined whether TMEM127 may serve to regulate baseline levels of the receptor.

Our findings reveal that TMEM127 loss leads to increased surface localization and reduced lysosomal degradation of RET and that TMEM127 recruits NEDD4 to RET (Figure 7F). NEDD4-mediated ubiquitination has been associated preferentially with K63 linkage, a modification that is coupled with nonproteasomal outcomes, including trafficking and degradation by the lysosome.[56,57,64] This is consistent with our observation that RET lysosomal localization is restored in TMEM127-KO cells reconstituted with WT-TMEM127 but not by a mutant that prevents TMEM127 recruitment of NEDD4 to RET. As RET

ubiquitination is implicated in multiple signaling events, including internalization, sorting, and trafficking,[45,53] the specific step(s) in which TMEM127 is involved will require additional investigation.

Multiple E3 ligases can target the same substrate,[55,56] and CBL, a member of the RING-E3 ligases, has also been associated with RET ubiquitination.[45,54] However, we found no evidence of TMEM127 interaction with CBL, suggesting that the actions of TMEM127 toward RET ubiquitination may be selective. However, as NEDD4 catalytically inactive mutant does not fully recapitulate TMEM127 loss, other members of the HECT-E3 ligases, such as WWP2,[8] may partner with TMEM127 to modulate target proteins. Besides the PY domains of TMEM127, the precise site(s) of association with RET and NEDD4 and specific determinants of how these interactions are regulated should be investigated in future studies.

While RET expression is tissue restricted,[9] TMEM127 is ubiquitously expressed,[1,2] suggesting that it may have other partners in tissues that do not express RET, as exemplified by its role with WWP2, in the degradation of MHC-II in *Salmonella*-infected cells,[8] and supportive of a broader role for TMEM127 in recruiting E3 ligases to distinct substrates in other cells. Of interest, this putative E3 ligase adaptor role might also be mechanistically involved in previously reported lysosomal and metabolic phenotypes that we reported in *Tmem127*-KO mice.[6,36] The nature of the target proteins and the specificities of the regulation of TMEM127-E3 ubiquitin ligase pairing in other tissues and cellular contexts remain to be investigated.

The role of E3 ubiquitin ligases in cancer has been previously recognized.[55] In the context of pheochromocytomas, the *VHL* tumor suppressor gene functions as the substrate-recognition pocket for CRL2, a member of the Cullin RING-E3 ubiquitin ligase complex.[65] $CRL2^{VHL}$ targets hypoxia-inducible factors (HIFs) HIF1α and HIF2α for degradation by the proteosome.[65] The HIF2α-encoding gene, *EPAS1*, is also mutated in pheochromocytomas, and loss-of-function mutations of *VHL* or gain-of-function mutations of *EPAS1* confer a characteristic transcription profile of aberrant activation of HIF and its downstream signals, known as pseudohypoxic/cluster 1 pheochromocytomas.[1] The molecular mechanisms of RET and TMEM127 reported in our study highlight the broader significance of the ubiquitin system in adrenomedullary cell tumorigenesis and extend it to the kinase group.

In summary, we have uncovered a relevant TMEM127 cellular target in pheochromocytomas and suggest that *TMEM127*-mutant tumors represent a previously unrecognized model of RET-related oncogenesis, which may be amenable to targeted therapy with clinical grade RET inhibitors.[66]

Limitations of the study

The lack of human pheochromocytoma cell lines to evaluate loss of TMEM127 is a limitation of our study. This work did not address how the RET-TMEM127-NEDD4 axis is engaged or terminated under physiological conditions. It is possible that other E3 ubiquitin ligases also contribute to RET regulation besides NEDD4, thus explaining that functional forms of NEDD4 expression do not fully recapitulate the RET accumulation levels found in cells lacking TMEM127. Other cellular factors required to enable a more complete

assessment of the regulation of the RET-TMEM127-NEDD4 axis may not have been present in our *in vitro* system. As effective commercial antibodies were not available to detect endogenous TMEM127 by confocal microscopy, we could not investigate its subcellular localization at the endogenous level.

STAR★METHODS

RESOURCE AVAILABILITY

Lead contact—Further information and requests for resources and reagents should be directed to the lead contact, Patricia L. Dahia, MD, PhD (dahia@uthscsa.edu).

Materials availability—This study did not generate new unique reagents.

Data and code availability—Bulk RNA-seq data and single nuclei RNAseq data from human tumors and mouse adrenals have been deposited at the Gene Expression Omnibus database and are available as of the date of publication. Accession numbers are listed in the key resources table. This paper does not report original code. Any additional information required to reanalyze the data reported in this paper is available from the lead contact upon request.

EXPERIMENTAL MODEL AND SUBJECT PARTICIPANT DETAILS

Human samples—Samples from 70 pheochromocytomas or paragangliomas confirmed histologically, were obtained from discarded tumor material from surgery, and from blood or saliva from patients who provided informed consent to participate in our repository study (NCT03160274), approved by the University of Texas Health Science Center at San Antonio institutional review board (IRB). This repository is open for enrollment of patients with pheochromocytoma and paraganglioma regardless of age, gender, ethnicity, race, or genotype.

DNA from germline or frozen tumors was isolated using standard method by Qiagen Genomic-Tip (Qiagen, Valencia, CA). All samples underwent genetic screening for pheochromocytoma/paraganglioma susceptibility genes using standard protocols based on Sanger sequencing or multiparallel sequencing.[67-69] A summary of the general features of these samples is shown on Table S1.

Additionally, we included both genotype and expression data from publicly available datasets from normalized data from our earlier cohorts (GSE2841 and GSE19987), and from the TCGA cohort (RNA-seq values quantified using HTSEQ-count for the TCGA PCPG cohort [3]were downloaded from the NCI Genomic Data Commons (GDC) Website.

Animals—Animal studies were performed under a protocol approved by the University of Texas Health San Antonio (UTHSA) IACUC (Institutional Animal Care and Use Committee), and in compliance with all relevant ethical regulations for animal testing and research. Mice with recombinant *Tmem127* allele (*Tmem127* fix) were generated by crossing *Tmem127* flx/+ mice with CMV-Cre transgenic mice of C57BL/6 J background (Tg(CMV-cre)1Cgn; Jackson Laboratory).[36] *Tmem127*$^{-/+}$ heterozygotes were mated to

obtain WT and KO mice. Adrenal glands were obtained from adult WT and KO mice, 10–11 months of age. Tissue was frozen at −80C until processed for Western blot, embedded in OCT, and sectioned at 4μm in a cryostat to process for confocal microscopy, or the nuclei were processed for single nuclei RNAseq. Process for Western blot, confocal microscopy, and single nuclei RNAseq are described in the respective subsections below.

Xenografts—SH-SY5Y-RET(WT)/CRISPR-control (TMEM127-WT) and SH-SY5Y-RET(WT)/CRISPR-TMEM127-T4 (TMEM127-KO) cells were diluted 1:1 into Geltrex (LDEV-Free RGF Basement Membrane Matrix, Gibco, A1413202) and inoculated subcutaneously (1×10^7 cells/0.2 mL/each) into the right flank of 5–7 week old nude mice (14 females and 13 males, Jackson Laboratories, #002019). Tumors were allowed to grow for 15 days, after which mice carrying TMEM127-KO cells were randomized into groups of 9 mice, each to receive vehicle or selpercatinib (30 mg/kg) intraperitoneally twice a day.[70] Tumors were measured with a caliper every other day[71,72] and tumor volume was estimated using the formula $V = (L \times W2) / 2$, where V is the tumor volume, L is the tumor length, and W is the tumor width. Mice were sacrificed after 8 days of treatment (24 days post inoculation), and tumors were dissected and weighed. Statistical analysis was performed using the two-sided Student's t-test (tumor volume *in vivo*) or Mann–Whitney test (tumor weight).

Cell lines—HEK-293FT cells (obtained from ThermoFisher/Invitrogen Cat#R70007) were cultured in Dulbecco's Modified Eagle's Medium (DMEM) supplemented with 10% fetal bovine serum (FBS) and 1% penicillin-streptomycin in a humidified 37°C incubator with 5% CO2. HEK-293FT *TMEM127*-KO cells were generated by using CRISPR/Cas9 lentiCRISPR v2, a gift from Feng Zhang (Addgene plasmid # 52961) using two separate guide RNAs targeting exons 2 (T2) and 4 (T4) of *TMEM127*, and stable polyclonal populations were selected with puromycin.[5,73]

SH-SY5Y neural crest derived human cell line of neuroblastoma lineage, a gift from Dr. Lois Mulligan and her lab at Queens University, Kingston, Ontario, Canada, originally obtained from ATCC (Cat#CRL-2266) were cultured in Dulbecco's Modified Eagle's Medium (DMEM) supplemented with 10% fetal bovine serum (FBS) and 1% penicillin-streptomycin in a humidified 37°C incubator with 5% CO2. SH-SY5Y *TMEM127*-KO cells were also generated by using the same constructs as those applied to HEK293FT cells above. Stable polyclonal populations were selected with puromycin or by GFP sorting (MSCV or GFP-expressing constructs).

SH-SY5Y RET KO cells have been previously reported and were a gift from Dr. Lois Mulligan.[62] TMEM127 guide RNAs targeting exons 2 and 4 were subcloned into pL-CRISPR.EFS.GFP, a gift from Benjamin Ebert[74] (Addgene plasmid #57818) and sorted by GFP to establish stable polyclonal populations.

HeLa cells were obtained from ATCC (Cat# CCL-2) were genetically modified using the TMEM127 guides above, cells stably expressing empty lentiCRISPR v2 (WT) and TMEM127 ex4 guide (KO-T4) were used for confocal experiments.

METHOD DETAILS

RNA-seq analysis—Total RNA was isolated using TRIzol reagent kit following the manufacturer's protocol (Invitrogen). Thirty samples were used for RNAseq processed at Novogene (Beijing, China). Sequencing libraries were generated using NEBNext Ultra TM RNA Library Prep Kit for Illumina (NEB, USA) using 1 μg of total RNA per tumor, following manufacturer's recommendations at Novogene. Paired-end clean reads were aligned to the reference genome (hg38) using STAR, HTSeq v0.6.1 was used to count the read numbers mapped for each gene, and fusion detection was performed using the STAR-Fusion.[13] Variant calling was performed with GATK HaplotypeCaller adjusted to a Phred-scaled confidence threshold of 20, as reported (https://github.com/gatk-workfiows/gatk3-4-rnaseq-germline-snps-indels). Summary information about the tumor samples is provided in Table S2.

Preparation of single-nuclei suspensions—The 'tween with salts and tris' (TST) method was used to isolate nuclei.[22] A fragment of approximately ~10-20mg of frozen pheochromocytoma tissue or a pair of mouse whole adrenals were placed into a well of a 6-well plate on ice with 1 mL of TST buffer (146 mM NaCl, 10 mM Tris-HCl pH 7.5, 21 mM MgCl2, 1 mM CaCl2, 0.03% Tween 20, 0.01% BSA in nuclease-free water). The tissue was then chopped using scissors for 10 min. The homogenized solution was then filtered through a 70 μm Falcon cell strainer, and additional 1 mL TST buffer was used to wash the cell strainer. Additional TST buffer was added to bring the total volume up to 5 mL. Sample was transferred into a 15 mL conical tube and centrifuged at 500g for 5 min at 4°C in a swinging bucket centrifuge, and the pellet was suspended in ST buffer (146 mM NaCl, 10 mM Tris-HCl pH 7.5, 21 mM MgCl2, 1 mM CaCl2 in nuclease-free water). The nuclei solution was filtered through a 35 μm Falcon cell strainer twice, stained with 4′9,6-diamidino-2-phenylindole (DAPI) and directly sorted using Flow Activated Nuclei/Cell Sorting with a FACSAriaII instrument. After sorting, the nuclei were suspended in NSB buffer (1XPBS without Mg2+ or Ca2+,1% BSA,0.2U/μL RNase Inhibitor) for immediate library construction using 10X Genomics.

SnRNAseq library generation and data preprocessing—snRNA-seq was performed with the 10x Genomics Chromium Single Cell 3′ Kit (v.3.3) according to standard protocol. Libraries were sequenced on an Illumina NovaSeq 6000 or NextSeq 550 sequencing platform. Cell Ranger v.5.0.0 (10x Genomics)[75] was used to align the sequencing reads to the hg38 human or mm10 mouse reference genome to build and distinguish cells from the background and generate count tables of unique molecular identifiers (UMIs) for each gene per cell, in which intronic counts were included.

For the human tumors, we captured a total of 40,645 single nuclei with high integrity, and a median of 2,044 genes was sequenced per nucleus (Table S2). An average of 49% of reads confidently mapped to introns and an average of 66% of reads mapped to a pre-mRNA reference transcriptome. Quality control parameters are displayed on Table S2.

For mouse adrenals we obtained a total of 21,274 nuclei ($\bar{x} = 3,900$ nuclei per WT and 3,345 nuclei per KO sample. Other parameters are displayed on Table S7.

snRNAseq data processing and quality control—The R package Seurat v.4.0.0 was used to calculate quality control metrics[76] Nuclei were removed from the downstream analysis if fewer than 500 distinct genes, or more than 20% or 5% of reads mapping to mitochondrial genes and ribosome genes were detected. Genes that were expressed in fewer than three cells were removed.

The Seurat package was also used for dimensionality reduction, clustering, and visualization. The count matrix was log normalized and multiplied by the scale factor 10,000. The Seurat FindVariableGenes function was used to define highly variable genes that were used as input to principal component analysis in which the top 2000 variable genes were chosen. Normalized data were scaled, and elbow plots were generated to determine which principal components to be used in the downstream analysis. Uniform manifold approximation and projection (UMAP) embeddings were calculated using these principal components as input and cells were clustered using the FindClusters function. Stable clusters were identified as clusters insensitive to small changes in the resolution parameter. Published postnatal human adrenal and neuroblastomas[26] or pheochromocytomas[18] were used as reference to classify cell types.

snRNAseq cell cycle analysis—Data from the chromaffin, SCP, stromal nuclei of human tumors and mouse cells were scored according to the expression of G2/M and S phase markers provided by Seurat in which Seurat CellCycleScoring function was applied.

snRNAseq gene set enrichment analysis (GSEA)—We used FindMarkers to find the genes that are different between WT and KO mouse clusters and *TMEM127* and *RET* tumor clusters (Log2FC > 0.5, BH-adj. P-value<0.05). Differentially expressed genes were used to run the pre-ranked GSEA analysis on the GSEA v4.3.2 provided by Molecular Signature Database (MSigDB) gene ontology gene sets,[77] and we considered significantly enriched those gene sets that met a threshold of normalized enrichment score (NES) > 1.5 or < −1.5 and Nominal p value <0.05.

snRNAseq copy number inference—R package InferCNV v.1.3.3 (cutoff = 0.1, denoise = TRUE) was processed, all cell types, except for chromaffin cells and SCPs, were used as reference cells. (inferCNV of the Trinity CTAT Project. https://github.com/broadinstitute/inferCNV)

Transcription factor activity analysis—The SCENIC analysis was run using default parameters[37] on mouse single nuclei that passed the filtering, using the 24-thousand motifs database for RcisTarget from https://resources.aertslab.org/cistarget/motif2tf/motifs-v9-nr.mgi-m0.001-o0.0.tbl. The input matrix was the normalized expression matrix output from Seurat.

SLICE analysis—Evaluation of differentiation potential (or entropy) of each nucleus from the chromaffin and SCP clusters was computed using the R package SLICE to order single nuclei by their differentiation potencies using default parameters.[78] One hundred iterations were used to calculate the entropy.

Cytotrace analysis—We used CytoTRACE (cellular trajectory reconstruction analysis using gene counts and expression) approach to recover the differentiation and maturation state of chromaffin cells and SCPs in our dataset.[33] We further visualized the maturation state of chromaffin cells and SCPs on the UMAP embeddings generated previously in Seurat.

Pseudotime trajectory analysis by Monocle3—The monocle3 R package[79] was used to generate chromaffin cells pseudotime trajectories. Nuclei were ordered in pseudotime using the learn graph, followed by the ordered cells' function. Based on the differentiation potential, the top 10 cells showing the highest entropy value in CC4 cluster were selected as the starting point for the trajectory.

RNA isolation and real-time PCR—Total RNA from human tumors, cell lines or mouse adrenals was isolated using TRIzol reagent kit following the manufacturer's protocol (Invitrogen). RNA was converted into cDNA using the High-Capacity cDNA Reverse Transcription kit and random hexamers (ThermoFisher) according to the manufacturer's instructions. Primer pairs were designed for human and mouse RET isoforms (see key resource table for sequences), and reference gene accordingly. SYBRGreen (Bio-Rad) was used for quantitative real-time PCR (qRT-PCR) in a QuantStudio6 instrument (ThermoFisher). Expression levels were calculated using the delta-delta Ct method.

Constructs, transfections, and transductions—The following constructs were purchased from VectorBuilder Inc (Illinois, USA) using a lentiviral backbone under a EF1A promoter (pLV): wild type RET 51 (NM_020975.6), RET 9 (NM_020630.6) carrying an MYC tag at the C terminus,[13] wild type C-CBL open reading frame carrying a V5 tag at the N terminus. Wild-type NEDD4 (#27002) and dominant negative, catalytically dead NEDD4-DD (#26999) open reading frames carrying an HA tag at the N terminus were obtained from Addgene and were a gift from Joan Massague.[58]

The TMEM127 constructs included: pEGFP-TMEM127, MSCV-N-Flag-TMEM127, and their respective empty vector controls (pEGFP-C2 and MSCV-empty vector) or pHM6-HA-TMEM127, have been previously reported.[2,5-7,73] Additional mutations of the TMEM127 and RET constructs were introduced using site-directed mutagenesis with MilliPore Sigma primers and Phusion polymerase.[13] A diagram depicting the various constructs is shown in Figures 5A and 6A.

Transfections of HEK293FT and HeLa were performed with Transit2020 (Mirus BioResearch) following standard manufacturer's protocols. For transient transfections, cells were harvested at 24h after transfection. Lentiviral particle generation was performed using standard procedures.[13] In brief, HEK-293FT cells were co-transfected with the pLV constructs above and the packing and envelope plasmids PAX2 (Addgene # 12260) and pMD2.G (Addgene #12259),[13] both gifts from Didier Trono. Supernatants were collected at 48h and 72h after transfection, centrifuged and strained. SH-SY5Y cells were transduced with viral particles and polybrene 8 μg/mL. Retroviral particles were generated by co-transfection of HEK293FT cells with retroviral constructs, along with

PKAT (Addgene #1215 and pCMV-VSVG #8454), gifts from Susan Lindquist[80] and Garry Nolan, respectively.

Cell line treatment—SH-SY5Y cells were exposed to various drugs, as follows: 100 μg/mL cycloheximide, 5 μg/ml brefeldin A, 100 nM bafilomycin A, 100 μM leupeptin, 25 μM chloroquine, 100nM bortezomib, and 5 μM retinoic acid, added to the media. Time frames of drug exposures are indicated in the text and/or figures and figure legends. Selpercatinib was used at 100nM as indicated in the text and figures.

For GDNF treatment, SH-SY5Y or HEK293FT cells were starved in an FBSfree medium for 3 h and treated with 100 ng/mL GDNF for the indicated times (10–30 min, as listed in the figure legends).

Cell lysate digestion with PnGase F: SH-SY5Y cell lysates, prepared using NP40 buffer as in the Immunoblot analysis section below, and were processed as follows: twenty μg of protein lysate (prepared as described in the Immunoblot analysis section below) were first denatured by addition of 1 μL of 10X Glycoprotein Denaturing Buffer (0.5% SDS, 40 mM DTT) and heated at 100°C for 10 min. After placing the denatured lysate on ice, 2 μL of 10X GlycoBuffer 2 (50 mM Sodium Phosphate, pH 7.5), 2 μL 1% NP-40 and 1μL PnGase F (500 units/μL) were digested at 37°C for 1 h. A loading buffer was added to stop the digestion and lysates were run on Western blot.

Immunoblot analysis—Lysates were obtained from frozen pheochromocytomas and paragangliomas, from frozen mouse adrenals and from the cell lines with a buffer containing 1% NP40, 50 mM Tris pH 8.0.150 mM NaCl, 10% glycerol, 2 mM EDTA and Halt Protease and Phosphate Inhibitor (ThermoFisher) after mechanical disruption, incubated on ice for 15 min and centrifuged at 4C for recovery of supernatant. Whole protein lysates were boiled in denaturing loading buffer (8% SDS, 0.4 M DTT, 0.2 M Tris-HCl, 4.3 M glycerol, 6 mM bromophenol blue), separated by SDS/polyacrylamide gel electrophoresis and transferred to polyvinylidene difluoride (PVDF) membrane at 110 V for 1–2 h at 4C. Membranes were blocked in 5% skim milk for 1 h, and then probed at 4°C overnight with the primary antibodies (see key source table). Blots were developed with chemiluminescent detection (Millipore Kit, cat WBKLS0500) on X-ray or captured on iBright imager CL1500 (Invitrogen/ThermoFisher). ImageJ (NIH) was used for quantification of the images.

Immunoprecipitation—Transfected HEK293FT cells were lysed in ice-cold NP40 lysis buffer (1% NP40, 50 mM Tris, 150 mM NaCl, 2 mM EDTA and 10% Glycerol) with EDTA-free protease inhibitor (Roche #11836170001). Lysates were cleared by centrifugation at 12,000 g at 4°C for 10 min. Cleared lysates were normalized for protein content by Bradford assay, and 2–3 mg of protein lysate were incubated with Dynabeads Protein G beads (Invitrogen cat 10003D) previously bound with the specific antibodies for 1h (GFP Santa Cruz Biotechnology cat #SC-9996; HA-tag Cell Signaling cat #3724S; HA-tag Bethyl Laboratories cat # A190-138A; RET Cell Signaling cat # 14698, or iso-species control IgG) at 4°C overnight on a rotator. The beads were washed three times with NP40 lysis buffer 15 min each at room temperature, eluted with 2 × Laemmli buffer by boiling at 100°C for 10

min and separated on SDS-PAGE, alongside corresponding whole cell lysates. Blots were probed with the relevant antibodies listed in the figure legends.

Endogenous IP was performed with SH-SY5Y WT or TMEM127- KO-T4 cells treated with 50μM chloroquine for 4h, and GDNF (100 ng/ml) for the last 15 min before harvesting; 1.5mg lysates were used for immunoprecipitation with 2μg RET antibody (Santa Cruz Technologies, cat # 101422) per 200μg lysates and processed as described above.

Ubiquitination pull-down—Ubiquitination of RET was detected using a Signal-Seeker Ubiquitination Detection Kit (BK161-S, Cytoskeleton) following the manufacturer's instructions. Transfected HEK293FT cells were washed in ice-cold PBS and collected in BlastR lysis buffer containing de-ubiquitination and SUMOylation inhibitor (N-ethylmaleimide and TPEN, NEM09BB) and protease inhibitor cocktail (PIC02). Cell lysates were collected using a BlastR filter and diluted with BlastR dilution buffer. One mg cell lysates were incubated with either control beads or ubiquitination affinity beads for 2 h at 4°C. Beads were washed with BlastR-2 wash buffer 3 times for 5 min each at 4°C, and then were centrifuged and incubated in bead elution buffer for exactly 5 min at room temperature. Eluates were collected in the spin columns, 2-mercaptoethanol (2 μL) was added to the samples, and then boiled for 5 min before running on SDS-PAGE.

Membrane and soluble fraction enrichment—Cells were scraped in lysis buffer (5 mM Tris with 5 mM EGTA and EDTA, PH = 8.0) containing proteinase inhibitors. Cell suspension was homogenized by passing through a needle 20 times and centrifuged at 1000 rpm to collect the supernatant. The postnuclear supernatant was transferred into 1.5 mL tubes and centrifuged at 35,000 rpm for 45 min. The supernatant is the soluble fraction, and the pellet is the membrane-enriched fraction. Sample buffer was added to each fraction and samples were boiled prior to SDS-PAGE running.

Immunofluorescence confocal microscopy—HeLa or SH-SY5Y cells were seeded onto coverslips and transfected or transduced accordingly, 24h or 48h later the cells were fixed using 4% formaldehyde for 10 min after media removal and two phosphate buffered saline (PBS) washes. The cells were permeabilized using 0.1% Triton X-100 (10 min, room temperature) and blocked with 2% bovine serum albumin (BSA) in 0.1% Triton X-100 for 1h at room temperature. The cells were then stained with appropriate primary antibodies overnight at 4°C, and washed in PBS, then incubated with secondary antibodies for 1 h at room temperature. For plasma membrane staining, 3ug/ml Wheat Germ Agglutinin (WGA, Cat#29026-1, Biotium) was used to stain the plasma membrane for 30 min at room temperature after fixation. The cells were washed with PBS and mounted on glass slides with 50% glycerol in PBS. Cells were imaged using a ZEISS LSM710 confocal microscope (×100, oil immersion objective).

Image analyses were performed with ImageJ software. Pearson's correlation coefficient was used to quantify the colocalization.[6] The extracellular background was subtracted from images using the Background Subtraction function in ImageJ. Pearson's correlation coefficient values were obtained from individual cells expressing the relevant markers in each experiment using the Coloc 2 ImageJ plugin (http://imagej.net/Coloc_2).

Immunohistochemistry—Briefly, tissue sections from pheochromocytoma or paraganglioma were processed on a Discovery Ultra Staining Module. Antigen retrieval was performed in Cell Conditioning 2 (citrate solution pH = 6.0) for 80 min and then incubated with Anti-Ret antibody [EPR2871] Abcam ab134100 at 1:400 dilution for 1h. Sections were then incubated with biotinylated anti-rabbit or anti-mouse antibody followed by streptavidin-peroxidase. Reaction was developed by 3,3′-diaminobenzidine (DAB) and counterstained with hematoxylin. Images were acquired under 200× magnification. H score was calculated by combining the signal intensity to the percentage of cells with positive signals as reported.[81] Mouse adrenals were processed using a similar approach.

Proliferation assays—Cell proliferation was evaluated through a [3-(4,5-dimethylthiazol-2-yl)-5-(3-carboxymethoxyphenyl)-2-(4-sulfophenyl)-2H-tetrazolium, inner salt] (MTS) bio reduction assay. SH-SY5Y cells of the relevant genotypes were seeded at 3×10^4 cells/well in 96- well plates and allowed to proliferate for 24h and 48h. 20 μL MTS/PMS solution (Cell Titer Glo 2.0, Promega) was added to each well containing 100μL of cells in culture medium. Cells were incubated for 2 h at 37°C in a humidified, 5% CO2 atmosphere. Absorbance at 490nm was read at a plate reader and calculated relative to the 0 h timepoint to indicate relative cell-viability.

QUANTIFICATION AND STATISTICAL ANALYSIS

Data analyses were performed with the GraphPad Prism software (version 9.2.0, GraphPad Software Inc), Python, and Excel (Microsoft), with Student's two-tailed t test or one-way ANOVA. $p < 0.05$ was considered significant. Xenograft assessment was performed using unpaired Student's t-test, unpaired Mann–Whitney test.

Supplementary Material

Refer to Web version on PubMed Central for supplementary material.

ACKNOWLEDGMENTS

We thank Jingruo Zhang for technical assistance and insightful discussions; Subramanyan Srikantan, Acacia Coker, Kizil Yusoof, and former lab members for their technical contributions; and the patients who have generously donated tissue samples. We also thank Richard Tothill and Aidan Flynn for sharing normalized data from the single-nucleus sequencing files reported in Zethoven et al.[18] We acknowledge the UTHSCSA Genomics, Optical Imaging, and Flow Cytometry Core Facilities supported by NIH-P30-CA54174 and the South Texas Research Laboratory (STRL) Histology-Immunohistochemistry Laboratory at UTHSCSA. P.L.M.D. is a recipient of funds from the NIH (GM114102 and CA264248), the NETRF, VHL Alliance, and UT System Star Awards and is the holder of the Robert Tucker Hayes Distinguished Chair in Oncology. R.C.T.A. acknowledges funding support from NIH-R01ES031522, NIH-R01GM140456, and I01BX001882 (Veterans Administration Merit Award). L.M.M. is supported by the Cancer Research Society of Canada (19439) and the Canadian Institutes of Health Research (MOP-142303). The content of this manuscript is the responsibility of the authors and does not necessarily represent the official views of the NIH or other funding sponsors.

INCLUSION AND DIVERSITY

We support inclusive, diverse, and equitable conduct of research.

REFERENCES

1. Dahia PLM (2014). Pheochromocytoma and paraganglioma pathogenesis: learning from genetic heterogeneity. Nat. Rev. Cancer 14, 108–119. 10.1038/nrc3648. [PubMed: 24442145]
2. Qin Y, Yao L, King EE, Buddavarapu K, Lenci RE, Chocron ES, Lechleiter JD, Sass M, Aronin N, Schiavi F, et al. (2010). Germline mutations in TMEM127 confer susceptibility to pheochromocytoma. Nat. Genet 42, 229–233. 10.1038/ng.533. [PubMed: 20154675]
3. Fishbein L, Leshchiner I, Walter V, Danilova L, Robertson AG, Johnson AR, Lichtenberg TM, Murray BA, Ghayee HK, Else T, et al. (2017). Comprehensive Molecular Characterization of Pheochromocytoma and Paraganglioma. Cancer Cell 31, 181–193. 10.1016/j.ccell.2017.01.001. [PubMed: 28162975]
4. Dahia PLM, Ross KN, Wright ME, Hayashida CY, Santagata S, Barontini M, Kung AL, Sanso G, Powers JF, Tischler AS, et al. (2005). A HIF1alpha regulatory loop links hypoxia and mitochondrial signals in pheochromocytomas. PLoS Genet. 1, 72–80. 10.1371/journal.pgen.0010008. [PubMed: 16103922]
5. Flores SK, Deng Y, Cheng Z, Zhang X, Tao S, Saliba A, Chu I, Burnichon N, Gimenez-Roqueplo AP, Wang E, et al. (2020). Functional Characterization of TMEM127 Variants Reveals Novel Insights into Its Membrane Topology and Trafficking. J. Clin. Endocrinol. Metab 105, e3142–e3156. 10.1210/clinem/dgaa396. [PubMed: 32575117]
6. Deng Y, Qin Y, Srikantan S, Luo A, Cheng ZM, Flores SK, Vogel KS, Wang E, and Dahia PLM (2018). The TMEM127 human tumor suppressor is a component of the mTORC1 lysosomal nutrient-sensing complex. Hum. Mol. Genet 27, 1794–1808. 10.1093/hmg/ddy095. [PubMed: 29547888]
7. Qin Y, Deng Y, Ricketts CJ, Srikantan S, Wang E, Maher ER, and Dahia PLM (2014). The tumor susceptibility gene TMEM127 is mutated in renal cell carcinomas and modulates endolysosomal function. Hum. Mol. Genet 23, 2428–2439. 10.1093/hmg/ddt638. [PubMed: 24334765]
8. Alix E, Godlee C, Cerny O, Blundell S, Tocci R, Matthews S, Liu M, Pruneda JN, Swatek KN, Komander D, et al. (2020). The Tumour Suppressor TMEM127 Is a Nedd4-Family E3 Ligase Adaptor Required by Salmonella SteD to Ubiquitinate and Degrade MHC Class II Molecules. Cell Host Microbe 28, 54–68.e7. 10.1016/j.chom.2020.04.024. [PubMed: 32526160]
9. Mulligan LM (2014). RET revisited: expanding the oncogenic portfolio. Nat. Rev. Cancer 14, 173–186. 10.1038/nrc3680. [PubMed: 24561444]
10. Santoro M, Carlomagno F, Romano A, Bottaro DP, Dathan NA, Grieco M, Fusco A, Vecchio G, Matoskova B, Kraus MH, and Di Fiore PP (1995). Activation of *RET* as a dominant transforming gene by germline mutations of MEN 2A and MEN 2B. Science 267, 381–383. [PubMed: 7824936]
11. Besset V, Scott RP, and Ibáñez CF (2000). Signaling complexes and protein-protein interactions involved in the activation of the Ras and phosphatidylinositol 3-kinase pathways by the c-Ret receptor tyrosine kinase. J. Biol. Chem 275, 39159–39166. [PubMed: 10995764]
12. Santoro M, Moccia M, Federico G, and Carlomagno F (2020). RET Gene Fusions in Malignancies of the Thyroid and Other Tissues. Genes 11, 424. 10.3390/genes11040424. [PubMed: 32326537]
13. Estrada-Zuniga CM, Cheng ZM, Ethiraj P, Guo Q, Gonzalez-Cantú H, Adderley E, Lopez H, Landry BN, Zainal A, Aronin N, et al. (2022). A RET::GRB2 fusion in pheochromocytoma defies the classic paradigm of RET oncogenic fusions. Cell Rep. Med 3, 100686. 10.1016/j.xcrm.2022.100686. [PubMed: 35858593]
14. Yao L, Schiavi F, Cascon A, Qin Y, Inglada-Pérez L, King EE, Toledo RA, Ercolino T, Rapizzi E, Ricketts CJ, et al. (2010). Spectrum and prevalence of FP/TMEM127 gene mutations in pheochromocytomas and paragangliomas. JAMA 304, 2611–2619. 10.1001/jama.2010.1830. [PubMed: 21156949]
15. Toledo SPA, Lourenço DM Jr., Sekiya T, Lucon AM, Baena MES, Castro CC, Bortolotto LA, Zerbini MCN, Siqueira SAC, Toledo RA, and Dahia PLM (2015). Penetrance and Clinical Features of Pheochromocytoma in a Six-Generation Family Carrying a Germline TMEM127 Mutation. J. Clin. Endocrinol. Metab 100, E308–E318. 10.1210/jc.2014-2473. [PubMed: 25389632]

16. Armaiz-Pena G, Flores SK, Cheng ZM, Zhang X, Esquivel E, Poullard N, Vaidyanathan A, Liu Q, Michalek J, Santillan-Gomez AA, et al. (2021). Genotype-Phenotype Features of Germline Variants of the TMEM127 Pheochromocytoma Susceptibility Gene: A 10-Year Update. J. Clin. Endocrinol. Metab 106, e350–e364. 10.1210/clinem/dgaa741. [PubMed: 33051659]

17. Castro-Vega LJ, Buffet A, De Cubas AA, Cascón A, Menara M, Khalifa E, Amar L, Azriel S, Bourdeau I, Chabre O, et al. (2014). Germline mutations in FH confer predisposition to malignant pheochromocytomas and paragangliomas. Hum. Mol. Genet 23, 2440–2446. 10.1093/hmg/ddt639. [PubMed: 24334767]

18. Zethoven M, Martelotto L, Pattison A, Bowen B, Balachander S, Flynn A, Rossello FJ, Hogg A, Miller JA, Frysak Z, et al. (2022). Single-nuclei and bulk-tissue gene-expression analysis of pheochromocytoma and paraganglioma links disease subtypes with tumor microenvironment. Nat. Commun 13, 6262. 10.1038/s41467-022-34011-3. [PubMed: 36271074]

19. Powers JF, Brachold JM, and Tischler AS (2003). Ret protein expression in adrenal medullary hyperplasia and pheochromocytoma. Endocr. Pathol 14, 351–361. [PubMed: 14739491]

20. Takaya K, Yoshimasa T, Arai H, Tamura N, Miyamoto Y, Itoh H, and Nakao K (1996). Expression of the RET proto-oncogene in normal human tissues, pheochromocytomas, and other tumors of neural crest origin. J. Mol. Med 74, 617–621. [PubMed: 8912182]

21. Miya A, Yamamoto M, Morimoto H, Tanaka N, Shin E, Karakawa K, Toyoshima K, Ishizaka Y, Mori T, and Takai S (1992). Expression of the ret proto-oncogene in human medullarythyroid carcinomasand pheochromocytomas of MEN 2A. Henry Ford Hosp. Med. J 40, 215–219. [PubMed: 1362408]

22. Slyper M, Porter CBM, Ashenberg O, Waldman J, Drokhlyansky E, Wakiro I, Smillie C, Smith-Rosario G, Wu J, Dionne D, et al. (2020). A single-cell and single-nucleus RNA-Seq toolbox for fresh and frozen human tumors. Nat. Med 26, 792–802. 10.1038/s41591-020-0844-1. [PubMed: 32405060]

23. Hanemaaijer ES, Margaritis T, Sanders K, Bos FL, Candelli T, Al-Saati H, van Noesel MM, Meyer-Wentrup FAG, van de Wetering M, Holstege FCP, and Clevers H (2021). Single-cell atlas of developing murine adrenal gland reveals relation of Schwann cell precursor signature to neuroblastoma phenotype. Proc. Natl. Acad. Sci. USA 118, e2022350118. 10.1073/pnas.2022350118. [PubMed: 33500353]

24. Becht E, McInnes L, Healy J, Dutertre C-A, Kwok IWH, Ng LG, Ginhoux F, and Newell EW (2018). Dimensionality reduction for visualizing single-cell data using UMAP. Nat. Biotechnol 37, 38–44. 10.1038/nbt.4314.

25. Yu G, Wang L-G, Han Y, and He Q-Y (2012). clusterProfiler: an R package for comparing biological themes among gene clusters. OMICS A J. Integr. Biol 16, 284–287.

26. Bedoya-Reina OC, Li W, Arceo M, Plescher M, Bullova P, Pui H, Kaucka M, Kharchenko P, Martinsson T, Holmberg J, et al. (2021). Single-nuclei transcriptomes from human adrenal gland reveal distinct cellular identities of low and high-risk neuroblastoma tumors. Nat. Commun 12, 5309. 10.1038/s41467-021-24870-7. [PubMed: 34493726]

27. Dong R, Yang R, Zhan Y, Lai HD, Ye CJ, Yao XY, Luo WQ, Cheng XM, Miao JJ, Wang JF, et al. (2020). Single-Cell Characterization of Malignant Phenotypes and Developmental Trajectories of Adrenal Neuroblastoma. Cancer Cell 38, 716–733.e6. 10.1016/j.ccell.2020.08.014. [PubMed: 32946775]

28. Castro-Vega LJ, Letouzé E, Burnichon N, Buffet A, Disderot PH, Khalifa E, Loriot C, Elarouci N, Morin A, Menara M, et al. (2015). Multi-omics analysis defines core genomic alterations in pheochromocytomas and paragangliomas. Nat. Commun 6, 6044. 10.1038/ncomms7044. [PubMed: 25625332]

29. Dahia PLM, Hao K, Rogus J, Colin C, Pujana MAG, Ross K, Magoffin D, Aronin N, Cascon A, Hayashida CY, et al. (2005). Novel pheochromocytoma susceptibility loci identified by integrative genomics. Cancer Res. 65, 9651–9658. 10.1158/0008-5472.CAN-05-1427. [PubMed: 16266984]

30. Furlan A, Dyachuk V, Kastriti ME, Calvo-Enrique L, Abdo H, Hadjab S, Chontorotzea T, Akkuratova N, Usoskin D, Kamenev D, et al. (2017). Multipotent peripheral glial cells generate neuroendocrine cells of the adrenal medulla. Science 357, eaal3753. 10.1126/science.aal3753. [PubMed: 28684471]

31. Guo M, Bao EL, Wagner M, Whitsett JA, and Xu Y (2017). SLICE: determining cell differentiation and lineage based on single cell entropy. Nucleic Acids Res. 45, e54. 10.1093/nar/gkw1278. [PubMed: 27998929]
32. Trapnell C, Cacchiarelli D, Grimsby J, Pokharel P, Li S, Morse M, Lennon NJ, Livak KJ, Mikkelsen TS, and Rinn JL (2014). Pseudotemporal ordering of individual cells reveals dynamics and regulators of cell fate decisions. Nat. Biotechnol 32, 381–386. [PubMed: 24658644]
33. Gulati GS, Sikandar SS, Wesche DJ, Manjunath A, Bharadwaj A, Berger MJ, Ilagan F, Kuo AH, Hsieh RW, Cai S, et al. (2020). Single-cell transcriptional diversity is a hallmark of developmental potential. Science 367, 405–411. 10.1126/science.aax0249. [PubMed: 31974247]
34. Crona J, Lamarca A, Ghosal S, Welin S, Skogseid B, and Pacak K (2019). Genotype-phenotype correlations in pheochromocytoma and paraganglioma. Endocr. Relat. Cancer 26, 539–550. 10.1530/ERC-19-0024. [PubMed: 30893643]
35. Favier J, Amar L, and Gimenez-Roqueplo AP (2015). Paraganglioma and phaeochromocytoma: from genetics to personalized medicine. Nat. Rev. Endocrinol 11, 101–111. 10.1038/nrendo.2014.188. [PubMed: 25385035]
36. Srikantan S, Deng Y, Cheng ZM, Luo A, Qin Y, Gao Q, Sande-Docor GM, Tao S, Zhang X, Harper N, et al. (2019). The tumor suppressor TMEM127 regulates insulin sensitivity in a tissue-specific manner. Nat. Commun 10, 4720. 10.1038/s41467-019-12661-0. [PubMed: 31624249]
37. Aibar S, González-Blas CB, Moerman T, Huynh-Thu VA, Imrichova H, Hulselmans G, Rambow F, Marine JC, Geurts P, Aerts J, et al. (2017). SCENIC: single-cell regulatory network inference and clustering. Nat. Methods 14, 1083–1086. 10.1038/nmeth.4463. [PubMed: 28991892]
38. Hadoux J, Desterke C, Féraud O, Guibert M, De Rose RF, Opolon P, Divers D, Gobbo E, Griscelli F, Schlumberger M, et al. (2018). Transcriptional landscape of a RETC634Y-mutated iPSC and its CRISPR-corrected isogenic control reveals the putative role of EGR1 transcriptional program in the development of multiple endocrine neoplasia type 2A-associated cancers. Stem Cell Res. 26, 8–16. [PubMed: 29197744]
39. Andrew SD, Capes-Davis A, Delhanty PJD, Marsh DJ, Mulligan LM, and Robinson BG (2002). Transcriptional repression of the RET proto-oncogene by a mitogen activated protein kinase-dependent signalling pathway. Gene 298, 9–19. 10.1016/S0378-1119(02)00919-8. [PubMed: 12406571]
40. Hickey JG, Myers SM, Tian X, Zhu SJ, V Shaw JL, Andrew SD, Richardson DS, Brettschneider J, Mulligan LM, and Mulligan LM (2009). RET-mediated gene expression pattern is affected by isoform but not oncogenic mutation. Genes Chromosomes Cancer 48, 429–440. [PubMed: 19226610]
41. Van de Sande B, Flerin C, Davie K, De Waegeneer M, Hulselmans G, Aibar S, Seurinck R, Saelens W, Cannoodt R, Rouchon Q, et al. (2020). A scalable SCENIC workflow for single-cell gene regulatory network analysis. Nat. Protoc 15, 2247–2276. 10.1038/s41596-020-0336-2. [PubMed: 32561888]
42. Tahira T, Ishizaka Y, Itoh F, Sugimura T, and Nagao M (1990). Characterization of ret proto-oncogene mRNA encoding two isofroms of the protein prodcut in a human neuroblastoma cell line. Oncogene 5, 97–102. [PubMed: 2181380]
43. Richardson DS, Lai AZ, and Mulligan LM (2006). RET ligand-induced internalization and its consequences for downstream signaling. Oncogene 25, 3206–3211. 10.1038/sj.onc.1209349. [PubMed: 16418724]
44. Hyndman BD, Gujral TS, Krieger JR, Cockburn JG, and Mulligan LM (2013). Multiple Functional Effects of RET Kinase Domain Sequence Variants in Hirschsprung Disease. Hum. Mutat 34, 132–142. 10.1002/humu.22170. [PubMed: 22837065]
45. Hyndman BD, Crupi MJF, Peng S, Bone LN, Rekab AN, Lian EY, Wagner SM, Antonescu CN, and Mulligan LM (2017). Differential recruitment of E3 ubiquitin ligase complexes regulates RET isoform internalization. J. Cell Sci 130, 3282–3296. 10.1242/jcs.203885. [PubMed: 28794017]
46. Powers JF, Schelling K, Brachold JM, Tsokas P, Schayek H, Friedman E, and Tischler AS (2002). High-Level Expression of Receptor Tyrosine Kinase Ret and Responsiveness to Ret-Activating Ligands in Pheochromocytoma Cell Lines from Neurofibromatosis Knockout Mice. Mol. Cell. Neurosci 20, 382–389. 10.1006/mcne.2002.1139. [PubMed: 12139916]

47. Powers JF, Evinger MJ, Zhi J, Picard KL, and Tischler AS (2007). Pheochromocytomas in Nf1 knockout mice express a neural progenitor gene expression profile. Neuroscience 147, 928–937. [PubMed: 17582688]
48. Richardson DS, Rodrigues DM, Hyndman BD, Crupi MJF, Nicolescu AC, and Mulligan LM (2012). Alternative splicing results in RET isoforms with distinct trafficking properties. Mol. Biol. Cell 23, 3838–3850. 10.1091/mbc.E12-02-0114. [PubMed: 22875993]
49. Hirata Y, Shimokawa N, Oh-hashi K, Yu Z-X, and Kiuchi K (2010). Acidification of the Golgi apparatus is indispensable for maturation but not for cell surface delivery of Ret. J. Neurochem 115, 606–613. 10.1111/j.1471-4159.2010.06966.x. [PubMed: 20796177]
50. Citterio C, Vichi A, Pacheco-Rodriguez G, Aponte AM, Moss J, and Vaughan M (2008). Unfolded protein response and cell death after depletion of brefeldin A-inhibited guanine nucleotide-exchange protein GBF1. Proc. Natl. Acad. Sci. USA 105, 2877–2882. 10.1073/pnas.0712224105. [PubMed: 18287014]
51. Mograbi B, Bocciardi R, Bourget I, Juhel T, Farahi-Far D, Romeo G, Ceccherini I, and Rossi B (2001). The sensitivity of activated Cys Ret mutants to glial cell line-derived neurotrophic factor is mandatory to rescue neuroectodermic cells from apoptosis. Mol. Cell Biol 21, 6719–6730. 10.1128/MCB.21.20.6719-6730.2001. [PubMed: 11564857]
52. Heuser J (1989). Effects of cytoplasmic acidification on clathrin lattice morphology. J. Cell Biol 108, 401–411. [PubMed: 2563729]
53. Crupi MJF, Yoganathan P, Bone LN, Lian E, Fetz A, Antonescu CN, and Mulligan LM (2015). Distinct Temporal Regulation of RET Isoform Internalization: Roles of Clathrin and AP2. Traffic 16, 1155–1173. 10.1111/tra.12315. [PubMed: 26304132]
54. Scott RP, Eketjäll S, Aineskog H, and Ibáñez CF (2005). Distinct turnover of alternatively spliced isoforms of the RET kinase receptor mediated by differential recruitment of the Cbl ubiquitin ligase. J. Biol. Chem 280, 13442–13449. 10.1074/jbc.M500507200. [PubMed: 15677445]
55. Scheffner M, and Kumar S (2014). Mammalian HECT ubiquitin-protein ligases: biological and pathophysiological aspects. Biochim. Biophys. Acta 1843, 61–74. 10.1016/j.bbamcr.2013.03.024. [PubMed: 23545411]
56. Boase NA, and Kumar S (2015). NEDD4: The founding member of a family of ubiquitin-protein ligases. Gene 557, 113–122. 10.1016/j.gene.2014.12.020. [PubMed: 25527121]
57. Persaud A, Alberts P, Amsen EM, Xiong X, Wasmuth J, Saadon Z, Fladd C, Parkinson J, and Rotin D (2009). Comparison of substrate specificity of the ubiquitin ligases Nedd4 and Nedd4-2 using proteome arrays. Mol. Syst. Biol 5, 333. 10.1038/msb.2009.85. [PubMed: 19953087]
58. Gao S, Alarcón C, Sapkota G, Rahman S, Chen PY, Goerner N, Macias MJ, Erdjument-Bromage H, Tempst P, and Massagué J (2009). Ubiquitin ligase Nedd4L targets activated Smad2/3 to limit TGF-beta signaling. Mol. Cell 36, 457–468. 10.1016/j.molcel.2009.09.043. [PubMed: 19917253]
59. Kim HC, and Huibregtse JM (2009). Polyubiquitination by HECT E3s and the determinants of chain type specificity. Mol. Cell Biol 29, 3307–3318. 10.1128/MCB.00240-09. [PubMed: 19364824]
60. Lauwers E, Jacob C, and André B (2009). K63-linked ubiquitin chains as a specific signal for protein sorting into the multivesicular body pathway. J. Cell Biol 185, 493–502. [PubMed: 19398763]
61. Wirth LJ, Sherman E, Robinson B, Solomon B, Kang H, Lorch J, Worden F, Brose M, Patel J, Leboulleux S, et al. (2020). Efficacy of Selpercatinib in RET-Altered Thyroid Cancers. N. Engl. J. Med 383, 825–835. 10.1056/NEJMoa2005651. [PubMed: 32846061]
62. Crupi MJF, Maritan SM, Reyes-Alvarez E, Lian EY, Hyndman BD, Rekab AN, Moodley S, Antonescu CN, and Mulligan LM (2020). GGA3-mediated recycling of the RET receptor tyrosine kinase contributes to cell migration and invasion. Oncogene 39, 1361–1377. 10.1038/s41388-019-1068-z. [PubMed: 31645646]
63. Burnichon N, Vescovo L, Amar L, Libé R, de Reynies A, Venisse A, Jouanno E, Laurendeau I, Parfait B, Bertherat J, et al. (2011). Integrative genomic analysis reveals somatic mutations in pheochromocytoma and paraganglioma. Hum. Mol. Genet 20, 3974–3985. 10.1093/hmg/ddr324. [PubMed: 21784903]

64. Erpapazoglou Z, Walker O, and Haguenauer-Tsapis R (2014). Versatile Roles of K63-Linked Ubiquitin Chains in Trafficking. Cells 3, 1027–1088. [PubMed: 25396681]
65. Kaelin WG (2018). The von Hippel–Lindau Tumor Suppressor Protein. Annu. Rev. Cell Biol 2, 91–109. 10.1146/annurev-cancer-bio-030617-050527.
66. Thein KZ, Velcheti V, Mooers BHM, Wu J, and Subbiah V (2021). Precision therapy for RET-altered cancers with RET inhibitors. Trends Cancer 7, 1074–1088. 10.1016/j.trecan.2021.07.003. [PubMed: 34391699]
67. Toledo RA, Qin Y, Cheng ZM, Gao Q, Iwata S, Silva GM, Prasad ML, Ocal IT, Rao S, Aronin N, et al. (2016). Recurrent Mutations of Chromatin-Remodeling Genes and Kinase Receptors in Pheochromocytomas and Paragangliomas. Clin. Cancer Res 22, 2301–2310. 10.1158/1078-0432.CCR-15-1841. [PubMed: 26700204]
68. Flores SK, Estrada-Zuniga CM, Thallapureddy K, Armaiz-Peña G, and Dahia PLM (2021). Insights into Mechanisms of Pheochromocytomas and Paragangliomas Driven by Known or New Genetic Drivers. Cancers 13, 4602. 10.3390/cancers13184602. [PubMed: 34572828]
69. NGS in PPGL NGSnPPGL Study Group; Toledo RA, Burnichon N, Cascon A, Benn DE, Bayley JP, Welander J, Tops CM, Firth H, Dwight T, et al. (2017). Consensus Statement on next-generation-sequencing-based diagnostic testing of hereditary phaeochromocytomas and paragangliomas. Nat. Rev. Endocrinol 13, 233–247. 10.1038/nrendo.2016.185. [PubMed: 27857127]
70. Solomon BJ, Tan L, Lin JJ, Wong SQ, Hollizeck S, Ebata K, Tuch BB, Yoda S, Gainor JF, Sequist LV, et al. (2020). RET Solvent Front Mutations Mediate Acquired Resistance to Selective RET Inhibition in RET-Driven Malignancies. J. Thorac. Oncol 15, 541–549. 10.1016/j.jtho.2020.01.006. [PubMed: 31988000]
71. Toledo RA, Qin Y, Srikantan S, Morales NP, Li Q, Deng Y, Kim SW, Pereira MAA, Toledo SPA, Su X, et al. (2013). In vivo and in vitro oncogenic effects of HIF2A mutations in pheochromocytomas and paragangliomas. Endocr. Relat. Cancer 20, 349–359. 10.1530/ERC-13-0101. [PubMed: 23533246]
72. Rai D, Kim S-W, McKeller MR, Dahia PLM, and Aguiar RCT (2010). Targeting of SMAD5 links microRNA-155 to the TGF-β pathway and lymphomagenesis. Proc. Natl. Acad. Sci. USA 107, 3111–3116. [PubMed: 20133617]
73. Deng Y, Flores SK, Cheng Z, Qin Y, Schwartz RC, Malchoff C, and Dahia PLM (2018). Molecular and phenotypic evaluation of a novel germline TMEM127 mutation with an uncommon clinical presentation. Endocr. Relat. Cancer 25, X3. 10.1530/ERC-17-0359e. [PubMed: 30030286]
74. Heckl D, Kowalczyk MS, Yudovich D, Belizaire R, Puram RV, McConkey ME, Thielke A, Aster JC, Regev A, and Ebert BL (2014). Generation of mouse models of myeloid malignancy with combinatorial genetic lesions using CRISPR-Cas9 genome editing. Nat. Biotechnol 32, 941–946. 10.1038/nbt.2951. [PubMed: 24952903]
75. Chen D, Chen H, Du Y, Zhu Z, Wang J, Geng S, Xiong C, Zheng Y, Hou C, Diao Q, and Guo R (2020). Systematic identification of circular RNAs and corresponding regulatory networks unveil their potential roles in the midguts of eastern honeybee workers. Appl. Microbiol. Biotechnol 104, 257–276. 10.1007/s00253-019-10159-9. [PubMed: 31754765]
76. Stuart T, Butler A, Hoffman P, Hafemeister C, Papalexi E, Mauck WM, Stoeckius M, Smibert P, and Satija R (2018). Comprehensive integration of single cell data. Preprint at bioRxiv. 10.1101/460147.
77. Liberzon A, Subramanian A, Pinchback R, Thorvaldsdóttir H, Tamayo P, and Mesirov JP (2011). Molecular signatures database (MSigDB)3.0. Bioinformatics27, 1739–1740. 10.1093/bioinformatics/btr260. [PubMed: 21546393]
78. Fang D, Gan H, Lee JH, Han J, Wang Z, Riester SM, Jin L, Chen J, Zhou H, Wang J, et al. (2016). The histone H3.3K36M mutation reprograms the epigenome of chondroblastomas. Science 352, 1344–1348. 10.1126/science.aae0065. [PubMed: 27229140]
79. Cooney JD, Lin AP, Jiang D, Wang L, Suhasini AN, Myers J, Qiu Z, Wölfler A, Sill H, and Aguiar RCT (2018). Synergistic Targeting of the Regulatory and Catalytic Subunits of PI3Kdelta in Mature B-cell Malignancies. Clin. Cancer Res 24, 1103–1113. 10.1158/1078-0432.CCR-17-2218. [PubMed: 29246942]

80. Nathan DF, and Lindquist S (1995). Mutational analysis of Hsp90 function: interactions with a steroid receptor and a protein kinase. Mol. Cell Biol 15, 3917–3925. 10.1128/mcb.15.7.3917. [PubMed: 7791797]

81. Flanagan MB, Dabbs DJ, Brufsky AM, Beriwal S, and Bhargava R (2008). Histopathologic variables predict Oncotype DX™ Recurrence Score. Mod. Pathol 21, 1255–1261. 10.1038/modpathol.2008.54. [PubMed: 18360352]

82. Kamitani T, Kito K, Nguyen HP, and Yeh ET (1997). Characterization of NEDD8, a developmentally down-regulated ubiquitin-like protein. J. Biol. Chem 272, 28557–28562. 10.1074/jbc.272.45.28557. [PubMed: 9353319]

83. Sanjana NE, Shalem O, and Zhang F (2014). Improved vectors and genome-wide libraries for CRISPR screening. Nat. Methods 11, 783–784. 10.1038/nmeth.3047. [PubMed: 25075903]

84. Subramanian A, Tamayo P, Mootha VK, Mukherjee S, Ebert BL, Gillette MA, Paulovich A, Pomeroy SL, Golub TR, Lander ES, and Mesirov JP (2005). Gene set enrichment analysis: a knowledge-based approach for interpreting genome-wide expression profiles. Proc. Natl. Acad. Sci. USA 102, 15545–15550. 10.1073/pnas.0506580102. [PubMed: 16199517]

85. Trapnell C, Cacchiarelli D, Grimsby J, Pokharel P, Li S, Morse M, Lennon NJ, Livak KJ, Mikkelsen TS, and Rinn JL (2014). The dynamics and regulators of cell fate decisions are revealed by pseudotemporal ordering of single cells. Nat. Biotechnol 32, 381–386. [PubMed: 24658644]

Highlights

- *TMEM127* loss of function leads to increased RET surface expression and activation
- TMEM127 recruits the NEDD4 E3 ligase to RET and promotes its ubiquitination
- NEDD4-mediated RET ubiquitination involves the TMEM127 C terminus
- Oncogenesis due to TMEM127 deficiency is responsive to RET inhibition

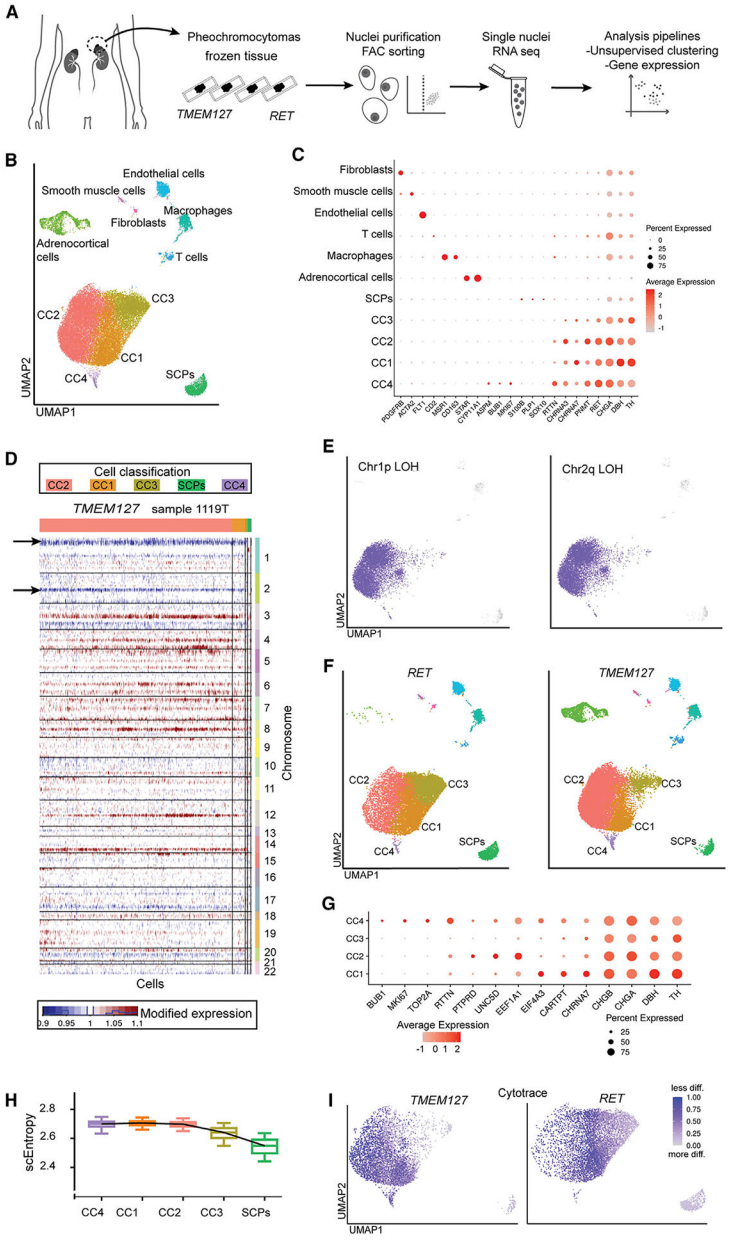

Figure 1. *TMEM127*- and *RET*-mutant tumors share transcriptional features at single-cell resolution

(A) Workflow of single-nucleus RNA-seq (snRNA-seq) processing of tumors with germline *TMEM127* (n = 3) and *RET* (n = 2) mutations.

(B) UMAP plot of cell types identified in snRNA-seq from the five PPGLs; the CC cluster is subdivided into four subclusters (CC1–4). SCP, Schwann-like cell positive; remaining cell types are labeled.

(C) Dot plot of markers that distinguish the clusters shown in (B), indicating the level and percentage expression per nuclei; expression scale represents *Z* score standard deviations from mean.

(D) Representative CNV heatmap with hierarchical clustering of results from inferCNV analysis of snRNA-seq of the indicated *TMEM127*-mutant tumor showing loss on chromosome (Chr) 1p and Chr 2q (arrows).
(E) UMAP embedding with annotation of the inferred CNV on Chr1p and Chr 2q loss from the tumor shown in (D).
(F) UMAP of the PPGL snRNA-seq split by genotype.
(G) Dot plot of selected markers in chromaffin clusters CC1–CC4; color represents scaled average expression of genes in each cell type, and the size indicates the proportion of cells expressing marker genes.
(H) The estimated entropy of chromaffin and SCP clusters using SLICE, ordered from highest (least stable) to lowest (most stable); boxplots represent median, first, and third quartiles of the distribution, and whiskers represent the highest and lowest data points within 1.5-interquartile range.
(I) Typical UMAP embedding of the cells by the scores calculated by CytoTRACE in *TMEM127*-mutant (left) and *RET*-mutant (right) samples.

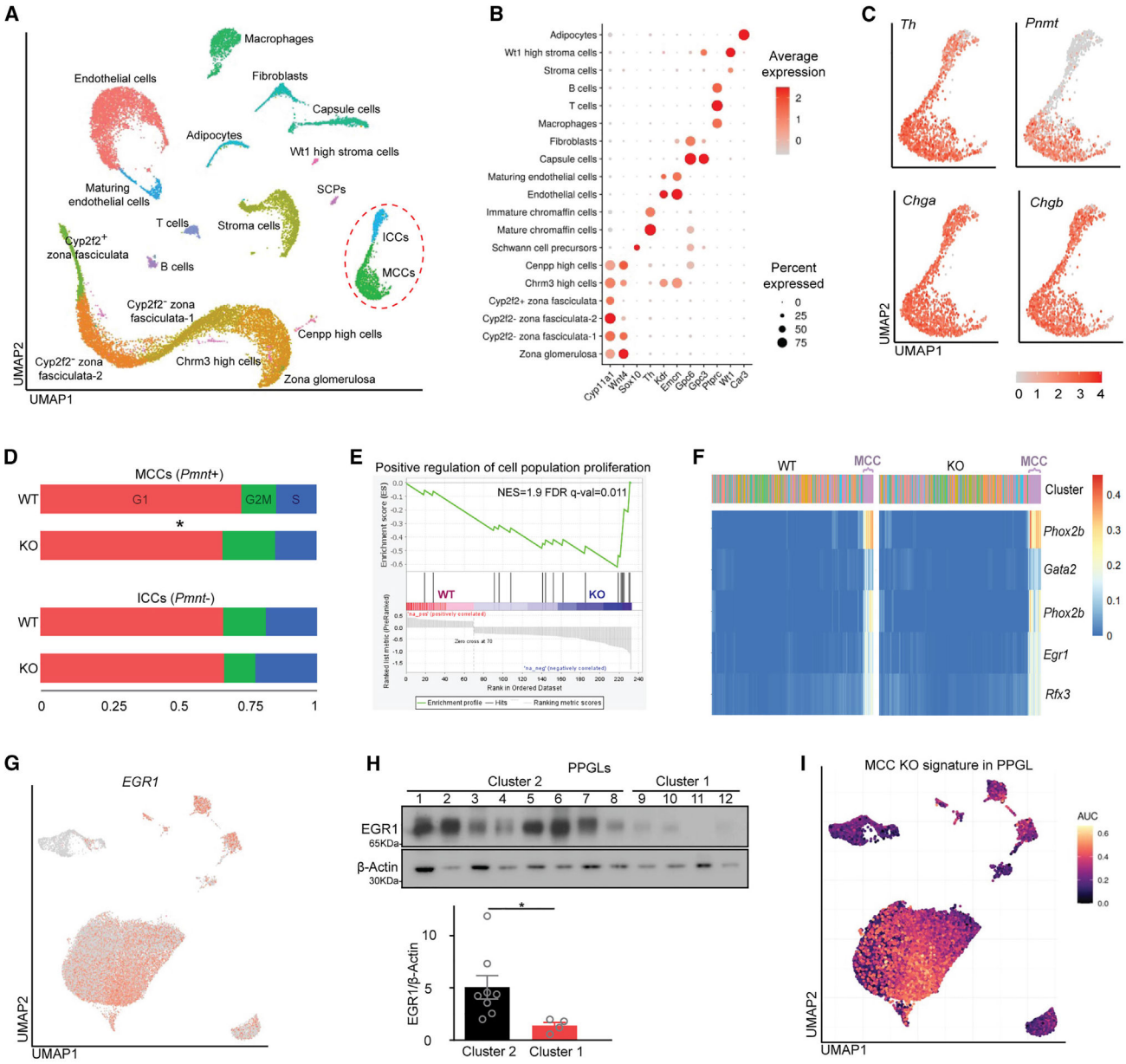

Figure 2. *Tmem127* deficiency in mouse adrenal preferentially affects MCCs

(A) UMAP plot of nuclei from six adrenals with indicated cell types; chromaffin clusters are indicated with a red dotted line.

(B) Dot plot depicting marker genes for adrenal cell types shown in (A).

(C) UMAP of *Th, Chga, Chgb*, and *Pnmt* expression in CCs.

(D) Proliferative profile of mature chromaffin (MCC, *Pnmt*$^{+}$) and immature chromaffin (ICC, *Pnmt*$^{-}$) nuclei from WT and KO samples, with G2/M phase markers higher in KO MCC; *p < 0.05, chi-squared test.

(E) Pre-ranked gene set enrichment analysis (GSEA) showing higher proliferative potential of KO MCC.

(F) Heatmap of predicted transcriptional factors revealed by SCENIC analysis in WT and KO mouse adrenal clusters and activated in MCC (indicated).
(G) UMAP plot of *EGR1* gene expression in TMEM127 and RET snRNA-seq (n = 5).
(H) Immunoblot analysis of EGR1 in 12 human pheochromocytoma/paragangliomas (PPGL) with mutations in Cluster2, *TMEM127* (lanes 1–3), *RET* (4–6), *NF1* (7), *HRAS* (8), and Cluster1, *SDHB* (9), *VHL* (10–110) and *EPAS1* (12), β-actin, loading control. EGR1 quantification grouped by cluster, data are mean ± SEM, *$p < 0.05$, two-tailed Student's t test.
(I) AUCell score plot of the mouse MCC-KO signature gene set in the human snRNA-seq dataset (highest expression = yellow).

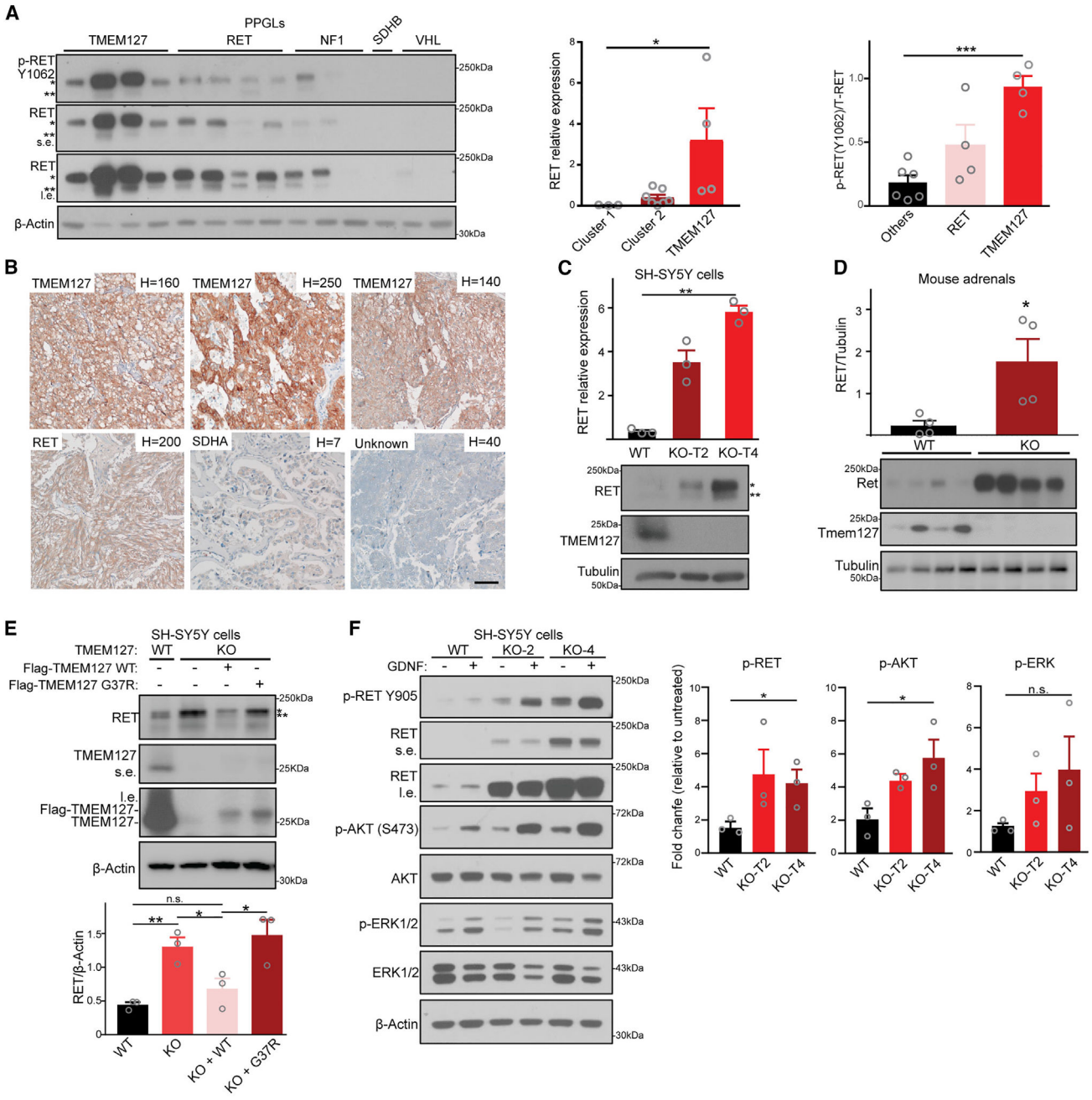

Figure 3. RET protein accumulates in TMEM127-deficient models

(A) Immunoblot of RET and phospho-RET(Y1062) in *TMEM127* mutant, *RET* mutant, and PPGLs with other mutations: n = 14 tumors, RET signal was quantified using ImageJ2, tumors were combined by genotype; TMEM127 (n = 4), other cluster 2 (RET, NF1, n = 6) or cluster 1 (SDHB, VHL, n = 3) are shown in the left graph, data are mean ± SEM, *p = 0.05, ANOVA. Quantification of p-RET (Y1062) over total RET from immunoblot analyzing lysates is shown in the right graph. Data are mean ± SEM, ***p < 0.001 by ANOVA; s.e., short exposure; l.e., long exposure.

(B) RET immunohistochemistry (IHC) staining of PPGLs of distinct genotypes, *TMEM127, RET, SDHA*, or unknown genotype (n = 6); H score is indicated for each tumor; scale bar, 50 μm.

(C) Immunoblot of RET, TMEM127, and tubulin in SH-SY5Y cells carrying intact (WT) or CRISPR-mediated TMEM127-KO using two sgRNAs targeting *TMEM127* (T2-KO and T4-KO), quantification of RET signals (n = 3 replicates), data are mean ± SEM, ***p = 0.0001 (two-tailed Student's t test)probed with RET, TMEM127, and tubulin.

(D) Immunoblot of WT and *Tmem127*-KO mouse adrenal lysates probed for RET, TMEM127, and tubulin; quantification performed as in (C), n = 4/genotype, data are expressed as mean ± SEM, *p < 0.05, two-tailed Student's t test.

(E) Immunoblot of SH-SY5Y control or TMEM127-KO cells before and after rescue with FLAG-tagged WT-TMEM127 construct or tumor-derived TMEM127 mutation (G37R); both constructs expressed at lower levels than endogenous TMEM127; blot was probed with RET, TMEM127, and tubulin; quantification of RET signals (n = 3 replicates), data are mean ± SEM, two-tailed Student's t tests:*p < 0.05, **p < 0.01, n.s., non-significant.

(F) Immunoblot of SH-SY5Y cells (WT, KO-T2, and KO-T4) serum starved for 3 h and exposed to GDNF (100 ng/mL) for 10 min and probed with RET, p-RET, AKT, p-AKT, ERK1/2, p-ERK1/2, and β-actin. Phospho-protein levels were quantified relative to their total and loading using ImageJ and are shown as fold change of GDNF/untreated, n = 3 replicates, data are mean ± SEM; *p < 0.05; n.s., nonsignificant (one-way ANOVA).

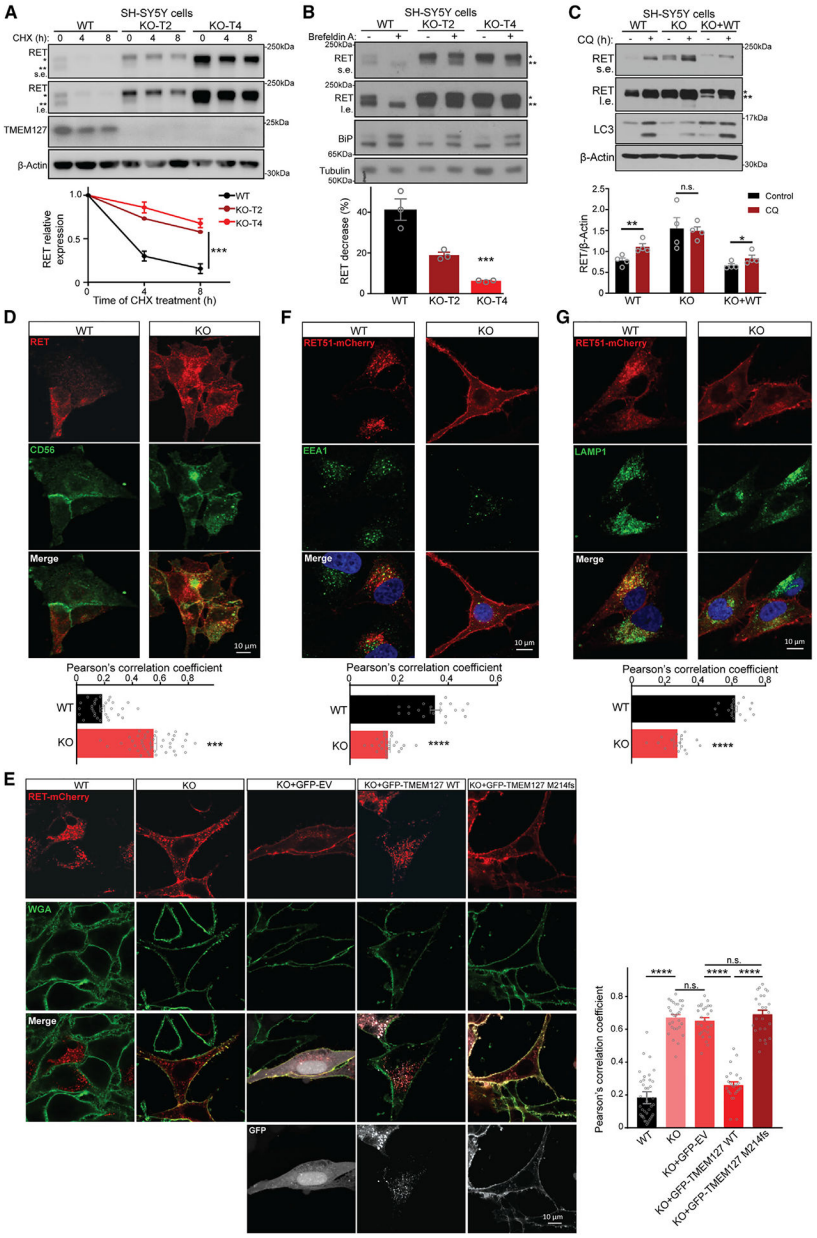

Figure 4. TMEM127 affects RET turnover, distribution, and lysosome-dependent degradation

(A) Immunoblots of lysates from SH-SY5Y *TMEM127*-WT, T2, or T4 KO cells treated with cycloheximide (CHX) at 100 μg/mL for 0, 4, and 8 h probed with RET, TMEM127, and tubulin; mature/fully glycosylated RET band (*175 kDa) and immature/partially glycosylated RET band (**155 kDa) are indicated; s.e., short exposure; l.e., long exposure; RET expression normalized by loading was quantified by ImageJ from n = 3 replicates, data are mean ± SEM, ***p < 0.001, two-way ANOVA.

(B) Immunoblots of lysates from SH-SY5Y *TMEM127*-WT, T2, or T4 KO cells treated with brefeldin A (5 μg/mL for 3 h) probed with RET, BiP, and tubulin; fully (*) and partially (**) glycosylated RET are indicated; RET expression was quantified from n = 3 replicates; data are mean ± SEM, ***p < 0.001, ANOVA.

(C) Immunoblots of lysates from SH-SY5Y *TMEM127*-WT, KO-T2 (KO), or T2 cells rescued with TMEM127-WT (KO + WT) treated with 25 μM chloroquine (CQ) for 0 and 4 h probed with RET and tubulin; RET expression was quantified (n = 3 replicates); data are mean ± SEM, two-tailed paired t tests, *p < 0.05, **p < 0.01; n.s., nonsignificant.
(D) Confocal microscopy of SH-SY5Y TMEM127-WT or KO cells, stained for endogenous RET (red), endogenous CD56 (green), and yellow (merged) shows colocalization between RET and CD56, calculated using Pearson's correlation coefficient (c.c., ImageJ) from three replicates and n = 32 WT and n = 43 KO cells; scale bar is indicated; data are mean ± SEM, two-tailed unpaired t test, p < 0.0001.
(E) Confocal microscopy of HeLa TMEM127-WT or KO cells transfected with RET-mCherry (red) and stained with WGA (green). KO cells were also transfected with empty GFP (GFP-empty vector [EV]), GFP-TMEM127-WT, or GFP-TMEM127-M214fs constructs (gray scale); merged images show yellow for RET/WGA colocalization; quantification was performed using Pearson's c.c. (n = 3 replicates); data collected from n = 38 WT, n = 30 KO, n = 27 KO+GFP-EV, n = 25 KO + GFP-TMEM127-WT, n = 25 KO + GFP-TMEM127-M214fs cells; scale bar is indicated; data are mean ± SEM, two-tailed, unpaired t tests and Welch's ANOVA multiple comparisons, ****p < 0.0001; n.s., nonsignificant.
(F) Confocal microscopy of HeLa TMEM127-WT or KO cells transfected with RET-mCherry (red) and stained with endogenous EEA1 (green); merged images show yellow for RET/EEA1 colocalization; quantification performed using Pearson's c.c. (n = 3 replicates); data collected from n = 29 WT, n = 31 KO; scale bar is indicated; data are mean ± SEM, ****p < 0.0001, two-tailed unpaired t test.
(G) Confocal microscopy of HeLa TMEM127-WT or KO cells transfected with RET-mCherry (red) and stained with endogenous LAMP1 (green), merged yellow for RET/LAMP1 colocalization, quantification performed using Pearson's c.c. (n = 3 replicates), and data from n = 36 WT, n = 30 KO cells; data are mean ± SEM, ****p < 0.0001, unpaired t test; scale bar is indicated.

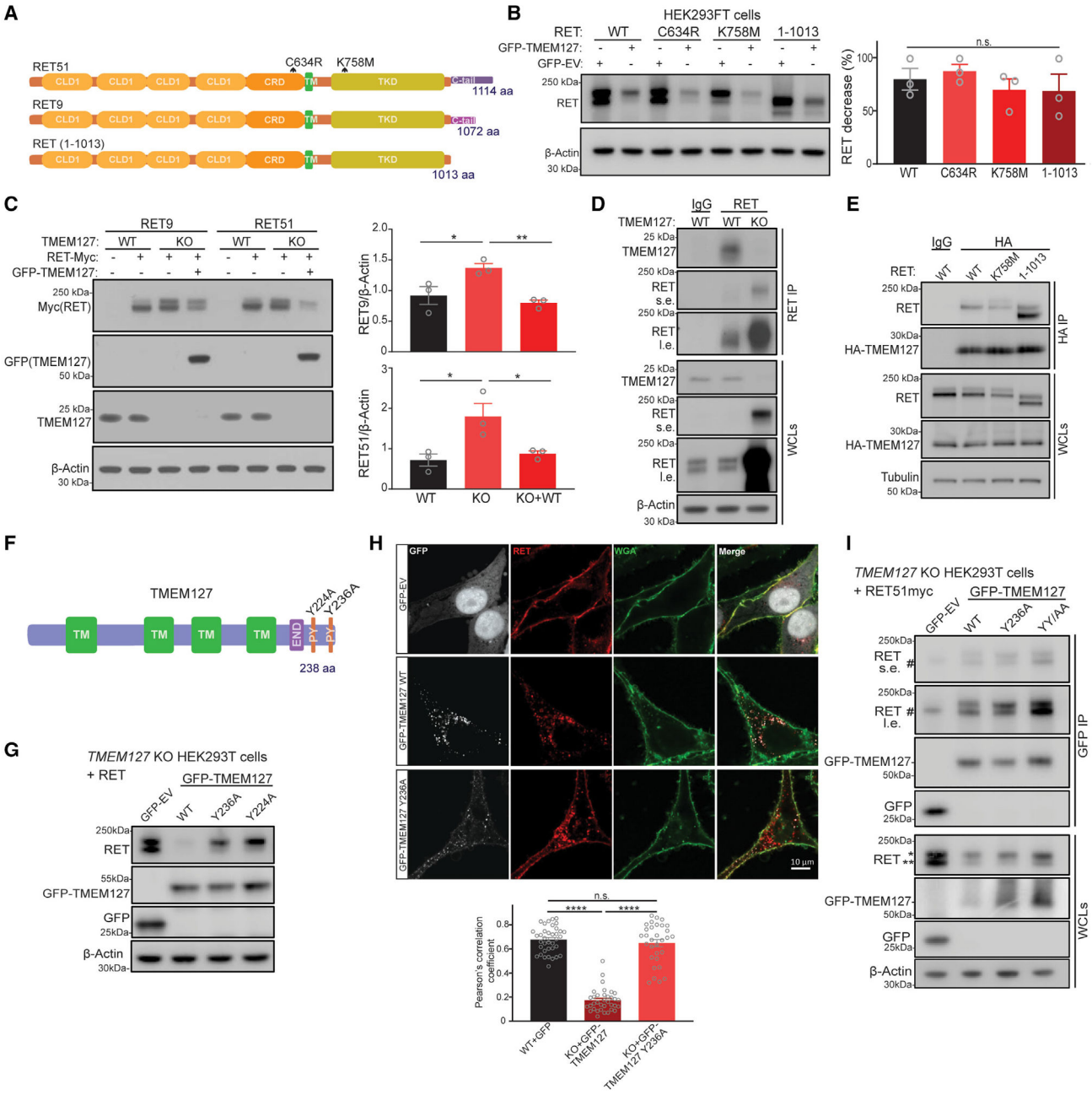

Figure 5. Mapping the interaction between TMEM127 and RET

(A) Diagram of RET functional domains and the RET constructs encoding WT RET9 and RET51 isoforms tagged with myc at the C terminus and three RET mutants: K758M, catalytically inactive mutant; C634R, oncogenic gain-of-function mutant; RET 1–1,013, truncated at 1,013 amino acids (aa); CLD, cadherin domain; CRD, cysteine-rich domain; TM, transmembrane domain; TKD, tyrosine kinase domain; C-tail, C terminus. RET length (aa) is depicted, arrows indicate mutation location.

(B) Immunoblots of HEK293FT cells transfected with RET-WT, C634R, K758M, and 1–1,013 and either GFP-TMEM127 or GFP-EV, probed with RET and β-actin. RET

expression normalized by loading was quantified by ImageJ (n = 3 replicates), data are mean ± SEM, two-tailed unpaired t test; n.s., nonsignificant.

(C) Immunoblot analysis of lysatesfrom *TMEM127*-WT or KO HEK293FT cells transfected with RET9-myc or RET51-myc with or without GFP-TMEM127; lysates were probed with myc (RET), TMEM127, and β-actin control. RET expression quantified by ImageJ (n = 3 replicates), data are mean ± SEM, two-tailed unpaired t tests, *p < 0.05, **p < 0.01.

(D) SH-SY5Y TMEM127-WT or KO cells (negative control) treated with 50 μM CQ for 4 h and GDNF for 15 min were harvested, and lysates were immunoprecipitated with a RET antibody overnight. Immunoprecipitates and whole-cell lysates (WCLs) were probed for TMEM127, RET, or β-actin; n = 2 replicates.

(E) HEK293FT cells transfected with RET51 WT, RET K758M, or RET51-1-1013 and co-transfected with HA-TMEM127 were immunoprecipitated with HA or control immunoglobulin (Ig) G; input WCL and IP samples were probed with RET and TMEM127 and β-actin (n = 3 replicates with HA- and GFP-TMEM127 pulldown).

(F) Diagram of *TMEM127* constructs, depicting the four transmembrane domains (TM), a C-terminal endocytic domain (END), and two distal PxxY motifs (PY); mutations are indicated.

(G) Immunoblot of lysates from HEK293FT *TMEM127*-KO cells co-transfected with RET51-myc and GFP-EV, GFP-TMEM127-WT (WT), GFPTMEM127 Y236A, GFP-TMEM127 Y224A, or double-mutant GFPTMEM127 Y224A/Y236A (YY-AA) (Y22246A), probed with RET, GFP, and β-actin; additional replicates and quantification shown in the related Figure S6A.

(H) Confocal microscopy of HeLa TMEM127-KO cells co-transfected with RET-mCherry (red) and empty GFP (GFP-EV), GFP-TMEM127-WT, or GFP-TMEM127-Y236A constructs (gray scale), stained with WGA (green); yellow shows RET/WGA colocalization, quantification performed using Pearson's c.c. (n = 3 replicates) from n = 37 KO + GFP-EV, n = 35 KO + GFP-TMEM127-WT, n = 31 KO + GFP-TMEM127 Y236A cells; data are mean ± SEM, ANOVA with multiple comparisons, ****p < 0.0001; scale bar is indicated.

(I) GFP IP of lysates from HEK293FT *TMEM127*-KO cells co-transfected with RET51-myc and GFP-EV, GFP-TMEM127-WT, GFP-TMEM127-Y236A, or GFPTMEM127-YY224/236AA (YY/AA); input and IP lysates were probed with RET, GFP, or β-actin; n = 3 replicates; #nonspecific binding of GFP.

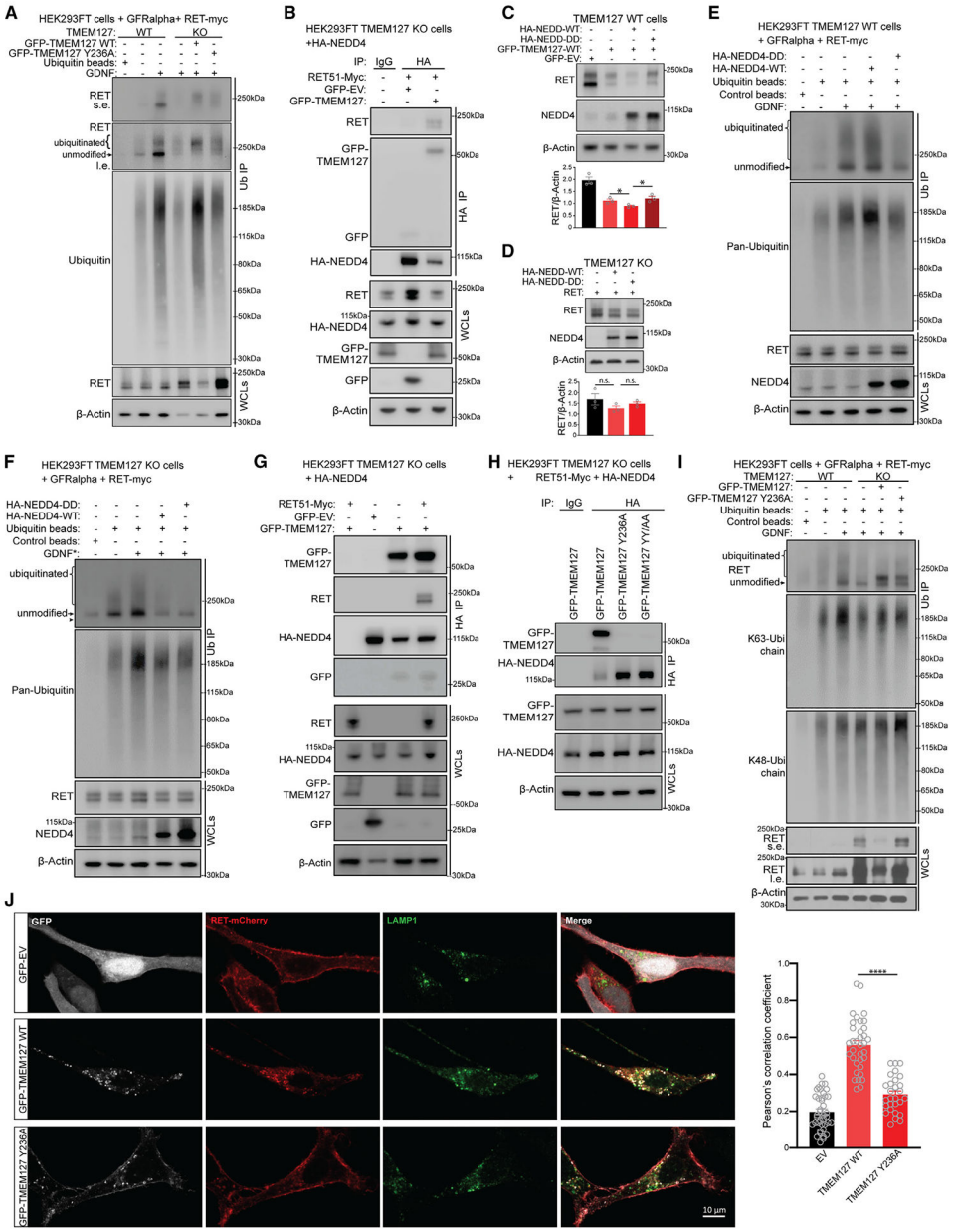

Figure 6. TMEM127 recruits NEDD4 to ubiquitinate RET

(A) HEK293FT *TMEM127*-WT and TMEM127-KO cells co-transfected with RET-MYC, GFRα1(GFRα), HA-ubiquitin, and either GFP-TMEM127-WT or GFPTMEM127-Y236A, stimulated or not with GDNF 100 ng/mL for 15 min; lysates were immunoprecipitated with ubiquitin beads or control beads and probed with RET and pan-ubiquitin; input lysates were probed with RET and β-actin; ubiquitinated RET and a band compatible with unmodified RET are indicated; n = 3 replicates.

(B) Lysates from HEK293FT *TMEM127*-KO cells transfected with RET51 and GFP or GFP-TMEM127-WT and HA-NEDD4 were immunoprecipitated with HA; IP lysates were probed with RET, NEDD4, and GFP; input lysates were probed with RET, NEDD4, GFP, TMEM127, and β-actin; n = 3 replicates.

(C) Immunoblot analysis of HEK293FT TMEM127-WT cells co-transfected with RET51-myc and GFP-EV or GFP-TMEM127-WT, and either NEDD4-WT or NEDD4-DD, and probed with RET, NEDD4, and β-actin; RET expression quantified by ImageJ (n = 3 replicates), data are mean ± SEM, two-tailed unpaired t tests, *p < 0.05.
(D) Immunoblot analysis of HEK293FT *TMEM127*-KO cells co-transfected with RET51-myc and either NEDD4-WT or NEDD4-DD and probed with RET, NEDD4, and β-actin; RET expression quantified by ImageJ, n = 3 replicates, data are mean ± SEM, two-tailed unpaired t tests; n.s., nonsignificant.
(E) Lysates from HEK293FT *TMEM127*-WT cells expressing RET51, GFRα1(GFRα), ubiquitin, and either HA-NEDD4-WT or HA-NEDD4-DD, stimulated with GDNF 100 ng/mL for 0 or 30 min, and immunoprecipitated with ubiquitin or control beads. IP lysates were probed with RET, NEDD4, and pan-ubiquitin; input lysates probed with RET- NEDD4 and β-actin (n = 2 replicates).
(F) Lysates from HEK293FT *TMEM127*-KO cells transfected with RET51, GFRα1(GFRα), HA-NEDD4, HA-NEDD4-DD, and ubiquitin stimulated with GDNF for 0 or 30 min and immunoprecipitated with ubiquitin or control beads; IP lysates were probed with RET, NEDD4, and pan-ubiquitin; input lysates probed with RET, NEDD4, and β-actin (n = 2 replicates).
(G) Lysates from 293FT *TMEM127*-KO cells transfected with HA-NEDD4, GFP-EV, and GFP-TMEM127-WT with or without RET-myc were immunoprecipitated with HA or unrelated IgG and probed with GFP(TMEM127), RET, HA(NEDD4), and β-actin (n = 2 replicates).
(H) HEK293FT *TMEM127*-KO cells co-transfected with RET51-myc, HA-NEDD4, and GFP-TMEM127-WT, GFP-TMEM127-Y236A, or GFP-TMEM127-Y224A/Y236A (YY/AA) were immunoprecipitated with HA; input and IP lysates were probed with GFP(TMEM127), RET, NEDD4, and β-actin (n = 3 replicates).
(I) HEK293FT *TMEM127*-WT and TMEM127-KO cells co-transfected with RET-myc, GFRα1(GFRα), HA-ubiquitin, and either GFP-TMEM127-WT or GFP-TMEM127-Y236A, stimulated or not with GDNF 100 ng/mL for 15 min (+); lysates were immunoprecipitated with ubiquitin beads; IP lysates were probed with RET, K63-linkage-specific polyubiquitin, and K48-linkage-specific polyubiquitin (n = 3 replicates).
(J) Confocal microscopy of HeLa TMEM127-KO cells transfected with RET-mCherry (red) GFP-TMEM127-WT, GFP-TMEM127-Y236A, or TMEM127-M214fs constructs (gray scale) and stained with LAMP1 (green) and yellow for RET/LAMP1 colocalization; quantification performed using Pearson's c.c. (n = 3 replicates) and n = 39 KO + GFP-EV, n = 35 KO + GFP-TMEM127-WT, and n = 28 KO + GFP-TMEM127-Y236A cells; data are mean ± SEM, unpaired t test, ****p < 0.0001; scale bar is indicated.

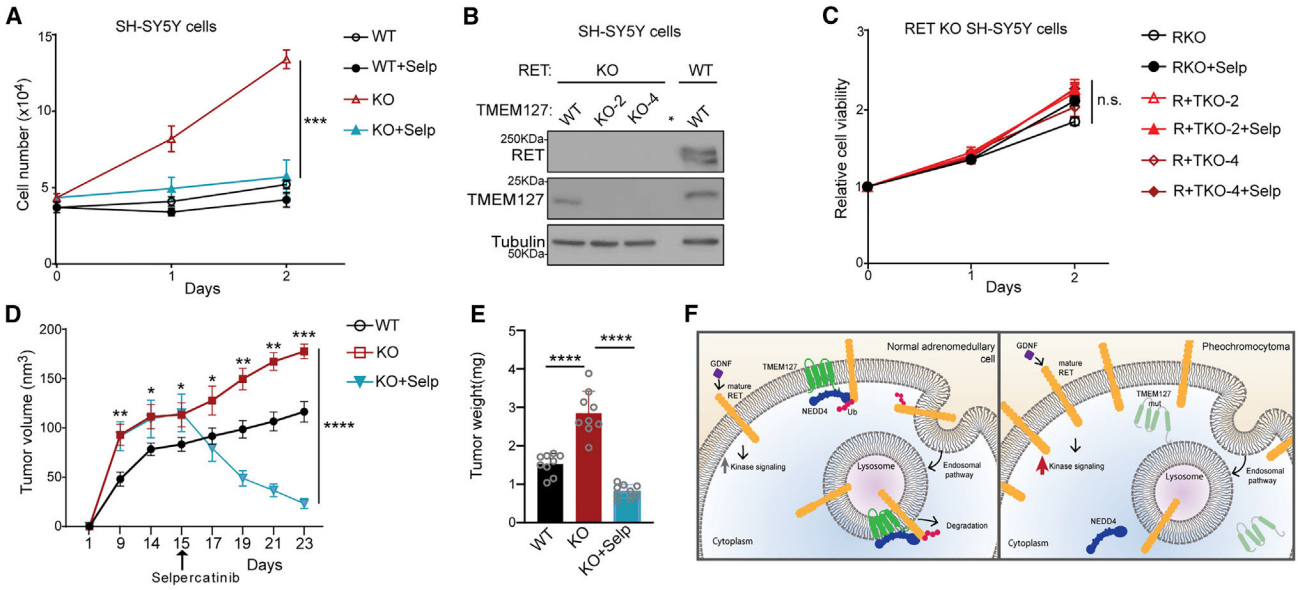

Figure 7. TMEM127 loss increases cell proliferation in a RET-dependent manner *in vitro* and *in vivo*

(A) Growth rate of SH-SY5Y TMEM127-KO and WT cells treated with vehicle or selpercatinib (selp) 100 nM, cells plated in triplicate, and counted daily for 3 days; experiments were repeated three times, data are mean ± SEM, ***p < 0.001, two-way ANOVA.

(B) Immunoblot representative of SH-SY5Y cell RET-KO or double RET- and TMEM127-KO from two TMEM127 guide RNAs, KO-2 and KO-4, an SH-SY5Y sample from WT-RET/WT-TMEM127 lysate shown as control; *blank lane; lysates were probed with RET, TMEM127, and tubulin.

(C) Relative viability of the cells indicated in (B): SH-SY5Y single RET-KO (RKO) cells or double RET/TMEM127 (R + T) KO-2 or KO-4 cells were treated with vehicle or selpercatinib (selp) 100 nM, plated in triplicate, and counted daily for 3 days; experiments were repeated two times; data are mean ± SEM data, relative to day 0, two-way ANOVA; n.s., nonsignificant.

(D) Tumor volume in nude mice engrafted subcutaneously with SH-SY5Y cells (TMEM127-WT, n = 9; TMEM127-KO, n = 18). At day 15 post injection, mice harboring TMEM127-KO tumor cells were randomized into two treatment groups, vehicle (n = 9) or selpercatinib (selp, n = 9) at 30 mg/kg twice/day intraperitoneally (i.p.) for 8 days; data are mean ± SEM; Student's t test, * = p ≤ 0.05, ** = p < 0.01, ***p < 0.001 (TMEM127-WT vs. TMEM127-KO all days; TMEM127-KO vs. TMEM127-KO + selp, day 23).

(E) Tumor weight was quantified after mice were sacrificed and tumors excised (n = 27); data are mean ± SD; Mann-Whitney test, ****p < 0.0001.

(F) Working model of the RET-TMEM127-NEDD4 axis in normal adrenomedullary cells and in pheochromocytomas with loss-of-function mutant TMEM127: in normal cells, TMEM127 recruits NEDD4 to RET and promotes RET internalization and trafficking to the lysosome, where it is degraded; loss or mutation of *TMEM127* leads to cell surface RET accumulation, signaling activation, and reduced lysosomal degradation.

KEY RESOURCES TABLE

REAGENT or RESOURCE	SOURCE	IDENTIFIER
Antibodies		
AKT	Cell Signaling Technology	Cat#9272; RRID: AB_329827
Alexa Fluor™ 647 Goat Anti-Rabbit SFX Kit, highly cross-adsorbed	Invitrogen	Cat#A31634, RRID:AB_2096814
BiP	Cell Signaling Technology	Cat#3177, RRID:AB_2119845
C-CBL	Cell Signaling Technology	Cat# 8447, RRID:AB_10860763
EGR1	Proteintech	Cat# 22008-1-AP, RRID:AB_11182923
EGR1	Cell Signaling Technology	Cat# 4153, RRID:AB_2097038
ERK1/ERK2	Cell Signaling Technology	Cat#4695; RRID: AB_390779
GAPDH	Cell Signaling Technology	Cat# 51332, RRID:AB_2799390
GFP	Santa Cruz Biotechnology	Cat# sc-9996, RRID:AB_627695
GFP/mCherry	Cell Signaling Technology	Cat#2956; RRID: AB_1196615
GFRα1	Novus Biologicals	Cat# NBP1-77043, RRID:AB_11035152
Goat anti-Mouse IgG (H + L) Cross-Adsorbed Secondary Antibody, Alexa Fluor 488	Invitrogen	Cat#A-11001; RRID: AB_2534069
GRB10	Cell Signaling Technology	Cat# 3702, RRID:AB_2112883
GRB2	Cell Signaling Technology	Cat# 36344, RRID:AB_2920901
HA-Tag	Bethyl	Cat# A190-138A, RRID:AB_2631894
HA-Tag	Cell Signaling Technology	Cat#3724; RRID: AB_1549585
K48-linkage Specific Polyubiquitin	Cell Signaling Technology	Cat# 8081, RRID:AB_10859893
K63-linkage Specific Polyubiquitin	Cell Signaling Technology	Cat# 5621, RRID:AB_10827985
LC3A/B	Cell Signaling Technology	Cat#4108; RRID:AB_2137703
LAMP1 (D4O1S)	Cell Signaling Technology	Cat# 15665, RRID:AB_2798750
MYC/c-Myc Antibody (9E10)	Santa Cruz Biotechnology	Cat#sc-40; RRID: AB_2857941
NEDD4	Cell Signaling Technology	Cat# 5344, RRID:AB_10560514
P53	ThermoFisher Scientific	Cat# MA5-12453, RRID:AB_11004789
Phosphorylated AKT-S473	Cell Signaling Technology	Cat#9271; RRID: AB_329825
Phosphorylated AKT-T308	Cell Signaling Technology	Cat# 4056, RRID:AB_331163
phosphorylated ERK T202/Y204	Cell Signaling Technology	Cat#4377; RRID: AB_331775
Phosphorylated RET-Y1062	Abcam	Cat# ab51103, RRID:AB_870738
Phosphorylated RET-Y905	Cell Signaling Technology	Cat#3221; RRID: AB_2179887
Purified anti-HA.11 Epitope Tag Antibody	BioLegend	Cat#901501; RRID: AB_2565006
RET (EPR2871)	Abcam	Cat# ab134100, RRID:AB_2920824
RET (D3D8R)	Cell Signaling Technology	Cat# 14698, RRID:AB_2798578
RET (8D10C9)	Santa Cruz Biotechnology	Cat#sc-101422; RRID: AB_2269605
RET E1N8X	Cell Signaling Technology	Cat#14556; RRID: AB_2798509
RET(E1N9A)	Cell Signaling Technology	Cat# 14699, RRID:AB_2798579
RET (8D10C9)	Santa Cruz Biotechnology	Cat# sc-101422, RRID:AB_2269605
SDHA	Cell Signaling Technology	Cat# 11998, RRID:AB_2750900
TMEM127	Bethyl Laboratories	Cat# A303-450A, RRID:AB_10952702
Ubiquitin	Santa Cruz Biotechnology	Cat# sc-8017, RRID:AB_628423

REAGENT or RESOURCE	SOURCE	IDENTIFIER
α-Tubulin	Cell Signaling Technology	Cat#3873; RRID: AB_1904178
β-Actin	Cell Signaling Technology	Cat#3700; RRID: AB_2242334
Wheat Germ Agglutinin (WGA)	Biotium	Cat#29026-1
EEA1	Cell Signaling Technology	Cat#3288, RRID:AB_2096811
EGR1	Cell Signaling Technology	Cat# 4153, RRID:AB_2097038
CD56	ThermoFisher Scientific	Cat# MA5-11563, RRID:AB_10985168
Bacterial and virus strains		
ONE SHOT STBL3 COMP E COLI	Invitrogen	Cat#C737303
Lentivirus	This paper	N/A
Biological samples		
Human pheochromocytoma or paraganglioma samples	This paper	N/A
Mouse adrenals (C57BL/6 mice)	This paper	Strain code:027
Chemicals, peptides, and recombinant proteins		
Fetal Bovine Serum	Gibco	Cat#26140079
DAPI (4′,6-Diamidino-2-Phenylindole, Dilactate)	ThermoFisher Scientific	Cat#EN62248
TrypLE Select, 10x	ThermoFisher Scientific	Cat#A1217701
Brefeldin A	Millipore-Sigma	Cat# B6542
Cycloheximide	Millipore-Sigma	Cat#01810-1G
Bafilomycin A1	Millipore-Sigma	Cat#19-148
Chloroquine	Millipore-Sigma	Cat#C6628
Leupeptin	Millipore-Sigma	Cat#62070
Bortezomib	Millipore-Sigma-Calbiochem	Cat#5.04314
MG132	Millipore-Sigma	Cat#M7449-1ML
Human GDNF (glial-derived neurotrophic factor)	Preprotech	Cat#450-10-100UG
PnGase F	New England Biolabs	Cat#P0704S
TransIT 2020	Mirus BioResearch	Cat#MIR5400
Polybrene	Millipore-Sigma	Cat#H9268
TRIzol	Invitrogen	Cat#15596018
Geltrex (LDEV-Free RGF Basement Membrane Matrix)	Gibco	Cat#A1413202
Selpercatinib	Chemietek	Cat#LOXO-292
Critical commercial assays		
NEBNext® Ultra TM RNA Library Prep Kit for Illumina	New England BioLabs	Cat#E7760L
High-Capacity cDNA Reverse Transcription Kit	Applied Biosystems	Cat#4368814
Phusion High-Fidelity PCR Master Mix with GC Buffer	ThermoFisher Scientific	Cat#F532L
iQ SYBR Green Supermix	Bio-Rad	Cat#1708880
Ubiquitin IP Assay	Cytoskeleton, Inc	Cat#BK161-S
Dynabeads™ Protein G beads	Invitrogen	Cat# 10003D
CellTiter-Glo® 2.0 Cell Viability Assay	Promega	Cat#G5421
Deposited data		
snRNAseq(mouse)	This paper	GSE218056
snRNAseq(human)	This paper	SRA-SUB12276788

REAGENT or RESOURCE	SOURCE	IDENTIFIER
bulk RNAseq	This paper	SRA-SUB12220510
Experimental models: Cell lines		
293FT Cell Line	Invitrogen	Cat#R70007
SH-SY5Y	ATCC, supplied by Dr. Lois Mulligan	Cat#CRL-2266
HeLa	ATCC	Cat# CCL-2, RRID:CVCL_0030
Experimental models: Organisms/strains		
Tmem127 mouse (C57/Bl/6) $^{tm1.1Pdah}$	Srikantan et al.[36]	MGI:5581337
Nu/J mouse	Jackson Laboratories	RRID:IMSR_JAX:002019
Oligonucleotides		
Primers for RT-PCR (sequence listed in Table S9)	Millipore Sigma	N/A
Recombinant DNA		
HA-ubiquitin	Kamitani et al.[82]	Addgene, Cat#18712
MSCV-GFP	Gift from Ricardo Aguiar, Qin et al.[2]	N/A
MSCV-N-Flag-TMEM127	Qin et al.[2]	N/A
MSCV-N-Flag-TMEM127-Y236A	This paper	N/A
pCDNA-GFRa1	Hyndman et al.[45]	N/A
pCI-HA-NEDD4	Gao et al.[58]	Addgene_27002
pCI-HA-NEDD4-DD	Gao et al.[58]	Addgene_26999
pEGFP-C2	Clontech	N/A
pEGFP-C2-TMEM127	Qin et al.[2]	N/A
pEGFP-C2- TMEM127-Y236A	This paper	N/A
pEGFP-C2-TMEM127-G37R	Flores et al.[5]	N/A
pEGFP-C2-TMEM127-Y224A	This paper	N/A
pEGFP-C2-TMEM127-Y224A,Y236A (YY/AA)	This paper	N/A
pEGFP-C2-TMEM127-M214FS	Flores et al.[5]	N/A
pHM6-HA-TMEM127	Qin et al.[2]	N/A
pLENTI-CRISPRv2	Sanjana et al.[83]	Addgene, Cat#52961
pL-CRISPR.EFS.GFP	Heckl et al.[74]	Addgene, Cat#57818
pLV-RET-1-1013	Estrada-Zuniga et al.[13]	N/A
pLV-RET51-c-Myc-C634R	Estrada-Zuniga et al.[13]	N/A
pLV-RET51-c-Myc-K758M	This paper	N/A
pLV[Exp]-Bsd- EF1A > hRET [NM_020630.6]/Myc	Estrada-Zuniga et al.[13]	N/A
pLV[Exp]-Hygro- EF1A > hRET [NM_020975.6]/Myc	Estrada-Zuniga et al.[13]	N/A
pMD2.G	A gift from Didier Trono Lab	RRID:Addgene_12259
psPAX2	A gift from Didier Trono Lab	RRID:Addgene_12260
RET-mCherry-pcDNA	Crupi et al.[53]	N/A
Software and algorithms		
Graph pad PRISM v9	Graphpad Prism Inc	https://www.graphpad.com/scientific-software/prism/
10x Cell Ranger v3	10x Genomics	https://support.10xgenomics.com/single-cell-gene-expression/software/pipelines/latest/what-is-cell-ranger

REAGENT or RESOURCE	SOURCE	IDENTIFIER
Gene Set Enrichment Analysis (GSEA)	Subramanian et al.[84]	https://www.gsea-msigdb.org/gsea/index.jsp
ImageJv1.51	NIH	https://imagej.nih.gov/ij/
inferCNV	Trinity CTAT Project	https://github.com/broadinstitute/inferCNV
Monocle 3	Trapnell et al.[85]	https://cole-trapnell-lab.github.io/monocle3/
Prism Software v.9.3.1	GraphPad Software Inc	N/A
R Studio v.4.1.0	RStudio	https://www.r-project.org/
Seurat v3.2.0	Stuart et al.[76]	https://satijalab.org/seurat/index.html
Slice	Guo et al.[31]	https://research.cchmc.org/pbge/slice.html
The Cancer Genome Atlas (TCGA) program	Broad firehose - version 2016_01_28	https://gdc.cancer.gov/access-data